Size and Shape Fluctuations of Large Unilamellar Vesicles as Investigated using Light Scattering

by

Elaine Lau

B.Sc., University of Toronto, 1992

A Thesis Submitted in Partial Fulfillment
of the Requirements for the Degree of
Master of Science
in the Department
of
Physics

SIMON FRASER UNIVERSITY
December 1994

APPROVAL

Name: Elaine Lau

Degree: Master of Science

Title of thesis: Size and Shape Fluctuations of Large Unilamellar Vesicles as Investigated Using Light Scattering

Examining Committee: Dr. Mike Plischke
Chair

Dr. Barbara Frisken
Senior Supervisor

Dr. John L. Bechhoefer
Department of Physics

Dr. Michael Wortis
Department of Physics

Dr. David Boal
Internal Examiner
Department of Physics

Date Approved: 8 December 1994

PARTIAL COPYRIGHT LICENSE

I hereby grant to Simon Fraser University the right to lend my thesis, project or extended essay (the title of which is shown below) to users of the Simon Fraser University Library, and to make partial or single copies only for such users or in response to a request from the library of any other university, or other educational institution, on its own behalf or for one of its users. I further agree that permission for multiple copying of this work for scholarly purposes may be granted by me or the Dean of Graduate Studies. It is understood that copying or publication of this work for financial gain shall not be allowed without my written permission.

Title of Thesis/Project/Extended Essay

Size and Shape Fluctuations of Large Unilamellar Vesicles as Investigated using light Scattering

Author: _____
(signature)

Elaine Lau
(name)

12 December 1994
(date)

Abstract

The techniques of dynamic and static light scattering were used to characterize the size and shape fluctuations of large unilamellar vesicles made with the extrusion technique. Attempts were made to manipulate fluctuation amplitudes and timescales by changing the temperature, viscosity, and excess surface area of the vesicles. By measuring the hydrodynamic radius of large unilamellar DMPC vesicles (d$\sim$ 100 nm) as a function of temperature, a sharp decrease of the radius was observed at 23°C and this was attributed to the gel transition. However, no fluctuations were observed with the change of temperature. To decrease the decay rate of the fluctuations to a timescale that is more easily detected, the viscosity was increased by suspending the vesicles in a glycerol solution. No shape fluctuation timescales were observed with the increase in viscosity. To enhance the amplitude of the fluctuations, the effective surface area of DEPC vesicles was increased by creating an osmotic pressure difference with NaCl across the bilayer which resulted in a decreased volume. Vesicle suspensions at 0%, 20%, 40%, and 75% volume-deflations were investigated. Aside from the timescale due to the translation of the vesicles, no other timescales were observed. The diffusion coefficient showed a scattering wavevector (q) dependence. By comparing the data to simulated results with a known polydisperse Schulz distribution, we can attribute this q-dependence to the polydisperse size distribution of the vesicles. The relative standard deviation of the diameter of the measured extruded vesicles was found to be 27%, much larger than expected. Unfortunately, one effect of the polydispersity is to obscure small amplitude changes of the shape of the vesicles. We believe that due to the combination of the polydispersity of the vesicle sample and the intrinsic small amplitude of the fluctuations, shape fluctuations in extruded vesicles of 100 nm can not be measured with these light scattering techniques.

Acknowledgments

I am extremely grateful for the continuing guidance and support of my committee and especially my supervisor, Barbara Frisken. I believe I was quite fortunate to work with such an interested and motivated individual.

I would like to thank Kim Christie for helping me to prepare my samples, and Art Bailey and Hu Gang for their help and hospitality during my visit to Exxon.

There are so many people that I would like to thank here at SFU for making life so pleasant. In particular, I would like to thank Dirk Jan Bukman for many useful discussions and distractions, Bradley Hughes, for his obliging computer genius and thoughts of anarchy, and Kevin Hewitt, for the emotional support that helped me to decide what I wanted out of life.

And finally, I must mention Andrew Datars, who was an important part of this thesis project, even though he was three time zones away.

Dedication

To my Grandmother

Contents

List of Figures

Chapter 1

Introduction

Artificial vesicles and membranes are among the few biological structures that can be described with simple physical models. In the case of the membrane, many of its properties can be modelled with a planar bilayer of molecules. One of the prime functions of the membrane in the cell is to act as a semi-permeable barrier to the outside world, and indeed, in laboratory experiments, the planar bilayer has been observed to selectively allow passage of substances across its width. Vesicles, which are "budded" from the membrane as illustrated in Fig. 1.1, can be modelled as a simple bilayer curved into a closed shape. Not surprisingly, physicists consider vesicles to be a useful model membrane system. Another aspect of vesicles that makes them interesting to researchers is the relative ease with which artificial vesicles can be produced in the laboratory. As such, vesicle experiments have been performed to investigate the osmotic properties of the bilayer (Hallett, 1993), the bending energy of the bilayer (Evans and Needham, 1987), adhesion properties, and phenomena such as shape fluctuations and budding. From a functional point of view, vesicles are responsible for the transport of proteins within the cell from the site where they are produced to the site where they are required. Biochemists, hoping to mimic nature, are developing artificial vesicles as carriers for drug delivery and attempting to mark the drug-carrying vesicles for particular destinations in the body.

Vesicles have the basic geometry of a hollow shell, with a certain amount of fluid inside. The shell consists of a bilayer of amphiphilic molecules and these molecules each consist of a hydrophilic "head" region and a hydrophobic "tail" region. Dispersed into solution, they may self-assemble into structures to shield the tails from contact with water. Hence, the molecules are brought into close contact via this hydrophobic effect. A common amphiphile

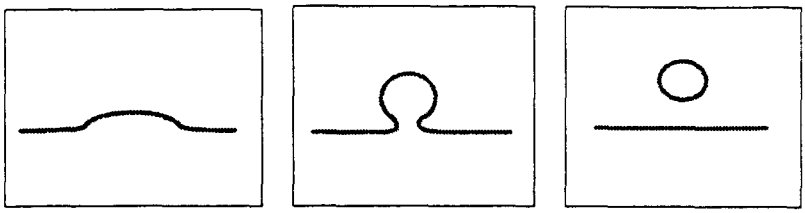

Figure 1.1: A very schematic picture of the budding process. The line represents the bilayer.

in the cell is the phospholipid, which has a head region connected by a phosphate group and a glycerol molecule to the double hydrophobic carbon chains in the tail region. Aside from vesicles, other self-assembled structures include micelles and planar bilayers, as shown in Fig. 1.2.

The property of the bilayer we are most interested in is its "stiffness". The quality of stiffness is characterized by a bending constant and is related to the energy required to bend the plane of the bilayer. It is generally believed that the shape of the vesicle, at biological temperatures and sizes, is governed for the most part by this bending energy (Helfrich, 1973). Since the bending energy for phospholipid bilayers is between 10 k_BT to 20 k_BT, (Evans and Needham, 1987), the bilayer can experience thermal fluctuations and this will result in shape fluctuations of the vesicle. The fluctuations are further constrained by the constant volume and surface area of the vesicle. This can be understood in terms of the energy scales involved: the energy required to bend the bilayer is is much smaller than the energy to change the surface area per lipid molecule and hence the surface area of the vesicle is conserved. The bending energy of the bilayer is also much smaller than either the energy needed to compress the fluid inside or outside of the vesicle. And, if the bilayer does not allow fluid transport across its width, so that the bilayer is impermeable on the time scale of the experiment and on the time scale of the shape fluctuation, the vesicle volume is considered constant. Thus the excess area, which is defined as the surface area of the vesicle less that of a sphere of the same volume, will characterize the fluctuations.

Shape fluctuations have been observed in so-called *giant* vesicles using video microscopy techniques, (Duwe et al., 1990). These giant vesicles, having diameters $\sim 10\,\mu$m, are roughly the size of the red blood cell in the body. They are made by the gentle hydration of dry phospholipid bilayers to produce vesicles that are a wide assortment of sizes with many that

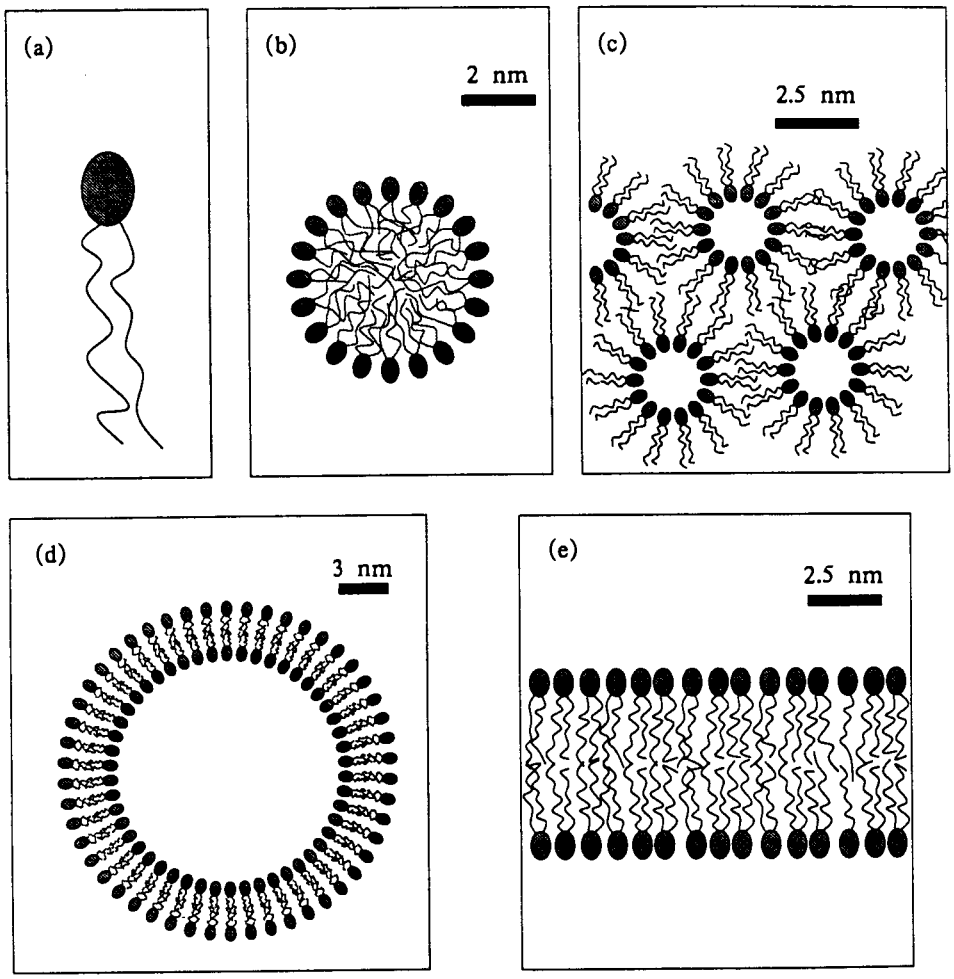

Figure 1.2: (a) A single amphiphile consisting of one hydrophilic head and two hydrophobic tails. Amphiphile self-assembled structures: (b) micelle, aqueous exterior with an oily interior; (c) inverted micelle, oily exterior with an aqueous interior; (d) vesicle, closed bilayer shell with aqueous exterior and interior; and (e) planar bilayer.

are multilamellar, i.e. consisting of multiple bilayers. Only those vesicles which appear to be unilamellar, that is they consist of a single bilayer, and which are considered to have an optimal excess area for fluctuations, are then isolated for study. Because stationary vesicles are desired for the microscope work, the fluid on the inside of the vesicle is made denser than that on the outside by washing the vesicles and then inserting them into a less dense medium. Thus, the vesicles will sink and translational motion will be inhibited. In the microscope, the cross-section of the vesicle defines a contour, which is observed to fluctuate about some time-averaged contour; it is this time dependence of the contour that is investigated. Results obtained for the bending constant are similar to ones obtained from planar bilayers. Although the microscopy technique is straightforward and the results agree with the predictions from theory, there are some inherent difficulties: the dynamics of the observed 2-D contour, essentially a cross-section, are difficult to extrapolate to the dynamics of the 3-D vesicle. Also, the optical and time resolutions are insufficient to see short length scale fluctuations, which may carry significant excess area (Milner and Safran, 1987). And while analysis is performed on roughly 40 different vesicles, the bias in the choice of vesicle may not result in a representative sample.

By examining a collection or an ensemble of vesicles, it may be possible to obtain better statistics of fluctuation measurements. Large unilamellar vesicles (LUVs), in which the diameter is 100nm, are roughly 100 times smaller than giant vesicles and have a number of advantages over the latter. Not only are LUVs easily produced in the laboratory with a relatively uniform size distribution, they have the additional relevance of being similar in size to the transport vesicles in cells. They are, however, too small to be viewed using microscopy techniques and must be examined with a technique that is sensitive to submicron length scales. As such, laser light scattering is the obvious choice for a suspension of these vesicles, since it is a probe of length scales comparable to vesicle size.

But first it is important to better understand the behaviour of a suspension of vesicles. If the suspension could be viewed in the microscope the individual vesicles would be seen to be moving incessently in a random fashion, a behaviour called Brownian motion, as illustrated in Fig. 1.3. This behaviour is caused by the constant bombardment of the vesicles by the fluid molecules as they move about randomly due to their thermal energy and this leads to the diffusion of the vesicles. As the vesicles diffuse, a characteristic decay time can be associated with the diffusion and is dependent upon the size and shape of the vesicles. Similarly, non-spherical vesicles may also have an observable tumbling motion and

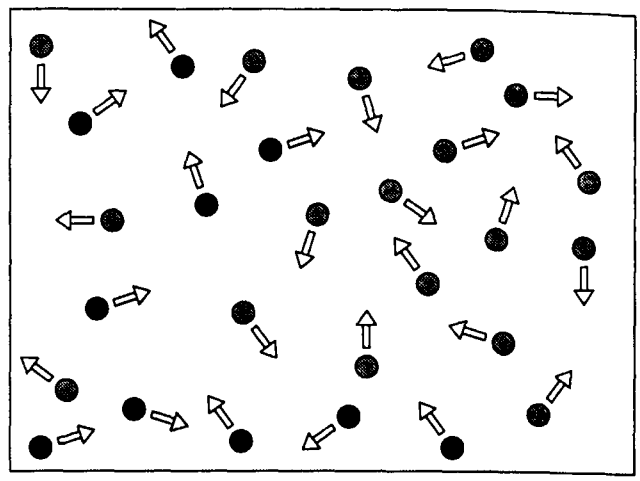

Figure 1.3: A schematic representation of the Brownian motion of vesicles, which are drawn as circles. The arrows indicate the instantaeous velocity.

a corresponding rotational diffusion decay time that depends on the degree of asymmetry. By modelling the vesicle bilayer as having a bending constant such that the bilayer is not rigid, one can easily imagine shape deformation of the vesicle as it undergoes translational diffusion. A decay time may then be associated with the relaxation to the original shape which is dependent upon the characteristic "stiffness" or bending constant of the bilayer, as shown in Fig. 1.4.

Shape fluctuations have been measured in the droplet phase of microemulsions, a physical system which is similar to vesicles; these emulsions consist of oil droplets coated with a single layer of soap, suspended in water. Fluctuations were first measured by Huang et al.(1987) from microemulsions of droplet size $\sim$100 Å using neutron spin-echo experiments, a form of neutron scattering. More recently, shape fluctuations of emulsions of a much larger droplet size $\sim$ 1μm, have been measured with diffusing wave spectroscopy (Gang et al., preprint). DWS is a technique of light scattering in the limit of a highly scattering sample, in which the light is scattered many times before exiting the sample.

By scattering light from a suspension of large unilamellar vesicles, we hope to measure shape and size fluctuations. But how is light scattering a probe of fluctuations? The scattered light is actually an interference pattern that results from the light scattered from each individual vesicle. Furthermore, as each vesicle diffuses or rotates or deforms, the

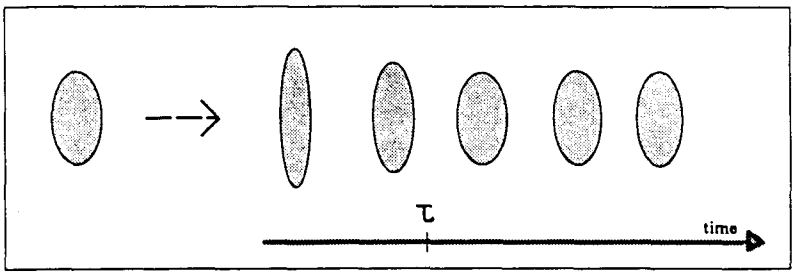

Figure 1.4: Timescale of possible shape deformation: The shapes represent one vesicle as it diffuses in time, with constant excess area. The left most shape is the time-averaged shape. The arrow indicates the push received from the fluid molecules which then results in the shape deformation. The shape then relaxes back to the time-averaged shape in time τ, which is the decay time for the fluctuation. After a time larger than τ, the vesicle receives another push from the fluid molecules, and the cycle is repeated.

interference pattern will change in time. By examining the time dependence of the scattered light, information about the dynamics of the vesicles can be obtained.

Two types of light scattering methods will be used: static light scattering and dynamic light scattering. Dynamic light scattering involves the correlation of the scattered intensity at a particular scattering wavevector. From a measurement of the intensity-intensity correlation function in time, information can be obtained about the characteristic decay times of the sample, with different types of motion having different characteristic decay times. From the decay time obtained for the translational diffusion, the hydrodynamic radius of the particles can be extracted. Additional decay times found may indicate either rotation or fluctuation of the vesicle. Static light scattering, however, is the measurement of the time-averaged intensity as a function of scattering wavevector, which is essentially the form factor of the particles. For spherical shells, this is the square of the zeroth order Bessel function, which has various maxima and minima. At a minimum, the intensity of the scattered light from the shell is dramatically decreased and, here, the signal from the fluctuations would be enhanced. Any dynamic light scattering measurements made at this particular scattering wavevector would be most sensitive to the fluctuations.

To briefly summarize the chapters in this thesis: the theory of light scattering is discussed in Chapter 2, specifically how the correlation function of the fluctuations in the sample

relates to the correlation function of the scattered intensity, and how the decay rate is related to the diffusion coefficient and the hydrodynamic radius for Brownian particles. In Chapter 3, the experimental apparatus and set-up, the sample preparation, and the experimental procedure of the light scattering experiments on vesicles are described. In Chapter 4, the general form of the experimental data measured is shown and the programs used to fit the data are described. The remainder of the chapter is a discussion of the effect of polydispersity on the data and the analysis. The experimental results from light scattering from vesicles are presented and analyzed in Chapter 5. Chapter 6 is a brief summary of this series of experiments, and a discussion of possible future work.

Chapter 2

Light Scattering and Vesicles

Light scattering is a useful non-invasive probe of submicron length scales. The light is scattered from all of the particles in the sample and the resulting interference pattern is analysed to obtain information about the particles' structure and dynamics. Appropriate samples are non-absorbing, non-magnetic and dielectric in character — with examples including fluid mixtures and suspensions of Brownian particles, such as the vesicles in which we are interested. This chapter is a brief description of how the light is scattered and in what way the scattered light relates to the sample, with an emphasis on scattering from Brownian particles.

2.1 Light Scattering Theory

The basic geometry of a light scattering experiment is shown in Fig. 2.1: from a coherent source such as a laser, light enters the scattering cell and is scattered in all directions by the sample. The position of the detector which measures the intensity of scattered light defines the scattering angle θ, and the intersection of the incident light beam and that of the scattered light intercepted by the detector is called the scattering volume.

The incident electric field can be described as a monochromatic plane wave,

$$\mathbf{E}_i(\mathbf{r},t) = \hat{\mathbf{n}}_i E_o e^{i(\mathbf{k}_i\cdot\mathbf{r}-\omega_i t)} \quad , \tag{2.1}$$

where $\hat{\mathbf{n}}_i$ is in the direction of the incident polarization of the electric field, E_o is the field amplitude, and ω_i is the angular frequency. The incident wavevector $\mathbf{k}_i$ points in the direction of propagation of the incident wave and has a magnitude of $|\mathbf{k}_i| \equiv \frac{2\pi n}{\lambda_i}$, where λ_i

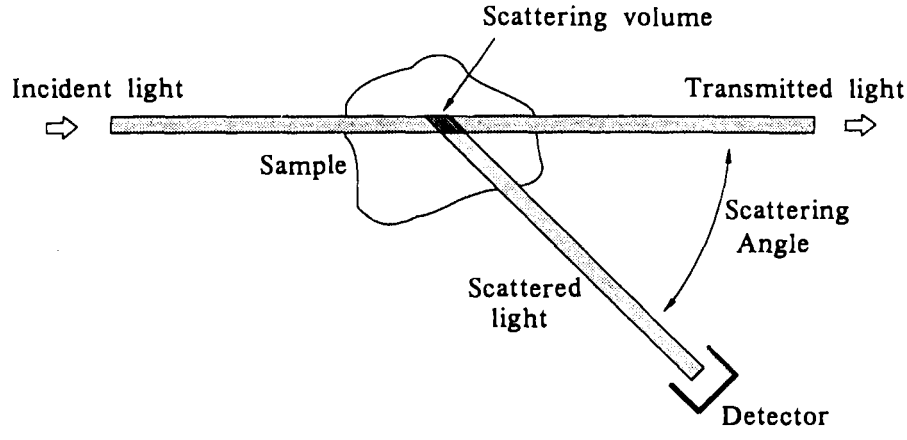

Figure 2.1: Basic light scattering geometry

is the wavelength of the incident light in vacuum and n is the index of refraction of the scattering medium.

An important quantity which is related to the geometry of the set-up and in particular to the scattering angle, is the scattering wavevector $\mathbf{q}$. It is the difference in wavevectors of the incident and the scattered light, with the latter pointing in the direction of propagation of the scattered wave intercepted by the detector. As little energy is absorbed or lost in quasi-elastic light scattering, the magnitudes of the incident and scattered wavelengths are comparable, and so $|\mathbf{k}_i| \simeq |\mathbf{k}_f|$. Then using conservation of momentum and the law of cosines, the magnitude of scattering wavevector is given by

$$|\mathbf{q}| \equiv |\mathbf{k}_i - \mathbf{k}_f| \simeq \frac{4\pi n}{\lambda} \sin(\theta/2) \quad , \tag{2.2}$$

where θ is the scattering angle between $\mathbf{k}_i$ and $\mathbf{k}_f$.

The scattering volume of the sample can be considered as a collection of many tiny subsections, with the size of each one being much smaller than a wavelength of light. As such, each subsection has a local density and in turn, a local dielectric constant which governs the response of the medium to the incident field. The local dielectric constant of the scattering medium can be represented as a sum of an average term and of a fluctuation term,

$$\epsilon(\mathbf{r}, t) = \varepsilon_o \mathbf{I} + \delta\epsilon(\mathbf{r}, t) \quad , \tag{2.3}$$

where **I** is a second rank identity tensor, and $\delta\epsilon$ is the tensor representing the fluctuations of the dielectric constant. Tensor quantities are required for a complete description because of the optical anisotropies characteristic of many particles. These anisotropies result in the so-called *depolarization* of the signal, i.e. there exists some component of the induced dipole moment not parallel to the applied field.

To the subsections of the sample, the effect of an incident light beam is that of an oscillating electric field and as each one experiences a force due to this field, charges are accelerated and oscillating dipoles are induced with the frequency of the incident light. From classical electromagnetic theory, an accelerated charge produces radiation of energy and in this instance, the radiation is simply the scattered light. Since each subsection can then be considered a source of scattered light, the scattered light as seen by the detector is actually an interference pattern resulting from interference from the radiated fields of different subsections.

From solving Maxwell's equations in a far-field approximation[1], the component of the scattered field with polarization $\hat{\mathbf{n}}_f$ is given by

$$\begin{aligned} E_s(R,t) &= -k_f^2 \frac{E_o e^{i(k_f R-\omega_i t)}}{4\pi\varepsilon_o R} \times \left[\int_v d^3r\, e^{i\mathbf{q}\cdot\mathbf{r}}\delta\varepsilon(\mathbf{r},t)\right]_{if} \\ &= -k_f^2 \frac{E_o e^{i(k_f R-\omega_i t)}}{4\pi\varepsilon_o R} \times \delta\varepsilon_{if}(\mathbf{q},t) \quad , \end{aligned} \tag{2.4}$$

where $\delta\varepsilon_{if}(\mathbf{q},t)$ is the component of the spatial Fourier transform of the dielectric constant fluctuation tensor, along the initial and final polarizations. Not only is the scattered field dependent upon the dielectric constant (density) fluctuations of the sample but the wavevector of the fluctuation that gives rise to the scattering is equal to the scattering wavevector.

As the local densities of the sample change due to thermal fluctuations, etc., the interference pattern will also change in a somewhat random manner in time, and this will result in a similar fluctuation of the scattered light. Correlation functions, which are a measure of the similarity or correlation of a property as it varies over time and/or space, can be used to characterize the fluctuations. The field-field correlation in time is written as

$$\langle E_s^*(R,0)E_s(R,\tau)\rangle = k_f^4 \frac{|E_o|^2}{16\pi^2\varepsilon_o^2 R^2} e^{-i\omega_i\tau}\langle\delta\varepsilon_{if}(\mathbf{q},0)\delta\varepsilon_{if}(\mathbf{q},\tau)\rangle \quad . \tag{2.5}$$

Hence the autocorrelation of the scattered field is directly proportional to the autocorrelation of the dielectric constant (density) fluctuations and, by finding the former using experimental

[1] A detailed derivation of the results from electromagnetic theory can be found in in Chapter 3 of Berne and Pecora (1976).

methods, information about the latter may also be inferred. This type of light scattering is referred to as dynamic light scattering or photon correlation spectroscopy.

Incidently, the temporal Fourier transform of the field-field correlation function is the power spectrum of the scattered light, which is the range of its frequency components. Interferometry, which is essentially the measurement of the frequency spectrum of scattered light intensity is then another method of detection and in such a way, the power spectrum of the density fluctuations of the sample can be measured. However, this method is not suitable for measuring vesicle shape fluctuations because, while the timescales of interest are in the the 1 kHz to 1 MHz range, while the incident wave is of $\sim 10^{14}$ Hz and a good interferometer can only measure $\Delta f/f = 10^{-6}$.

Static light scattering is the measurement of the total scattered light as a function of the scattering wavevector for a very narrow range of frequencies. Mathematically, it is the integral over time of the power spectrum for a particular q. As such, the scattered interference pattern will depend on the position of the particles in the sample, i.e. the structure factor, and the internal structure of the particles, i.e. the form factor. For example, a suspension of identical spheres will have a structure factor of unity because the spheres are randomly located, and the form factor of the square of the first order Bessel function. Howver, a suspension of spherical shells will have the form factor of the square of the zeroth order Bessel function. Hence, at the appropriate minima of the Bessel functions, the light scattered from the particles will be much diminished.

2.2 Scattering from Brownian Particles

Brownian particles were first observed in 1828 by Robert Brown as the incessant random motion of microscopic pollen grains. By scattering light from these particles and correlating the resulting interference pattern, information can be obtained about their size and shape. Assuming that the scattering particles are *monodisperse* in distribution, i.e. identical in size and in shape, the amount and polarization of the light scattered from an individual particle is determined by its molecular polarizability. This microscopic quantity is the collective measure of response of the molecules of the particle to an applied electric field and is therefore a property of the arrangement of the molecules and the overall shape of the particle. However, the polarizability can be affected by motion of the particle. For example, the re-orientation of a non-spherical particle due to rotational motion will result in some

depolarization of the scattered light, but the scattering due to translational motion of the particle will not.

It is important to assume first, that the particles are isotropic with an average polarizability, and second, that the size of the particles is small in comparison to the wavelength of light. In addition, since the amount of light scattered from these particles is a great deal more than from the density fluctuations of the suspending fluid and the time scales for the latter are also typically orders of magnitude smaller, the contribution from the fluid medium can be neglected for dynamic light scattering measurements. The detected scattered field is then proportional to the sum of the contribution scattered from each particle j in the scattering volume,

$$\mathbf{E}(\mathbf{q},t) \sim \sum_{j=1}^{N} \alpha^j e^{i\mathbf{q}\cdot\mathbf{r}_j} \quad , \tag{2.6}$$

where the total number of particles in the scattering volume is N, and α^j is average polarization of the jth particle. Using Eq. 2.6, the autocorrelation function of E can be expressed as

$$\langle E(\mathbf{q},0)E(\mathbf{q},\tau)\rangle \sim \langle \sum_{j=1}^{N} (\alpha^j)^2 e^{i\mathbf{q}\cdot[\mathbf{r}_j(0)-\mathbf{r}_j(\tau)]}\rangle \quad . \tag{2.7}$$

This expression can be simplified by assuming the particles to be statistically independent and identical so that the result of the summation over the scattering particles is a factor of N. Therefore,

$$\langle E(\mathbf{q},\tau)E(\mathbf{q},0)\rangle \sim \langle N\rangle \alpha^2 \langle e^{i\mathbf{q}\cdot[\mathbf{r}(0)-\mathbf{r}(\tau)]}\rangle \quad , \tag{2.8}$$

and the field-field correlation is expressed as a function that is dependent on three factors: the mean number of particles in the scattering volume, the polarizability of the particles, and the positions of the particles.

The exponential factor of Eq. 2.8 can be written as the mean value[2] of an exponential for some arbitrary distribution such that

$$\langle e^{i\mathbf{q}\cdot[\mathbf{r}(0)-\mathbf{r}(\tau)]}\rangle = \int d\mathbf{R}\, e^{i\mathbf{q}\cdot[\mathbf{r}(0)-\mathbf{r}(\tau)]} P_s(\mathbf{R},\tau) \quad , \tag{2.9}$$

where

$$P_s(\mathbf{R},\tau) \equiv \langle \delta(R - [\mathbf{r}_j(\tau) - \mathbf{r}_j(0)])\rangle \quad , \tag{2.10}$$

[2]The mean value of x is defined as

$$\langle x\rangle = \int x P(x) dx \quad ,$$

where P(x) is the probability distribution.

is a general probability distribution which describes the location of each particle in the scattering volume. A particle experiencing Brownian motion is modelled as executing a random walk consisting of many steps. Each step is independent of the previous step and is also equally likely to have any direction and so it is well known that the location of the particle can be described by a Gaussian distribution. For times long in comparison to the step time, the probability of a particle found at a distance r away at time t later is given by a simple Gaussian function,

$$P(r,t) = (4\pi Dt)^{-3/2} e^{-r^2/4Dt} \quad , \tag{2.11}$$

where D is the diffusion coefficient. Upon substitution into Eq. 2.9 and followed by substitution into Eq. 2.8, the result of the integral is given by

$$\langle E(\mathbf{q},0)E(\mathbf{q},\tau)\rangle \sim \langle N\rangle \alpha^2 e^{-Dq^2\tau} \quad . \tag{2.12}$$

And thus the correlation function obtained from Brownian particles shows an exponential relaxation in which the decay rate is dependent upon the diffusion coefficient of the particles.

This diffusion coefficient in combination with hydrodynamic relations can yield further information about the size and possibly the shape of the particles. The Einstein relation for the self-diffusion coefficient is

$$D = \frac{k_B T}{\xi} \quad , \tag{2.13}$$

where k_B is the Boltzmann constant, T is the temperature, and ξ is the friction constant. In the Stokes approximation,

$$\xi = 6\pi\eta r_\circ \quad , \tag{2.14}$$

where η is the viscosity and $r_\circ$ is the hydrodynamic radius of a sphere. Therefore, by finding the decay rate of the correlation function measured in experiment, the diffusion coefficient and the hydrodynamic radius of the Brownian particles can be calculated.

2.3 Shape Fluctuations

The vesicle is modelled as a thin hollow shell and can be thought of as a fluid droplet with constant volume and area. Its shape is determined by the bending energy of the bilayer as given by the Helfrich expression (Helfrich 1973) and any fluctuation of this shape can be described in terms of its deviation from a sphere. The work of Schneider, Jenkins, and

Webb (1984) on the hydrodynamics of droplet fluctuations determined the time rate of change of the droplet shape, and this theory was further extended to include the case of nonzero spontaneous curvature and the constraint of constant excess area by Milner and Safran (1987). The excess area is defined as the area of the droplet less that of the sphere of the same volume and it is this quantity that characterizes the fluctuations.

The contour of the droplet's surface is described by its distance from the chosen origin, which is located within the droplet,

$$r(\Omega) = r_o \left[1 + \sum_{l,m} u_{lm} Y_{lm}(\Omega) \right] \quad , \tag{2.15}$$

where Ω is the solid angle as measured from the vertical axis. The Y_{lm} are the spherical harmonics — a set of orthonormal functions over a unit sphere, and u_{lm} is the amplitude of the particular mode. r_o is a parameter that sets the lengthscale of the distorted shape.

By specializing to an axi-symmetric shape and assuming the equipartition of energy, the expression for the mean square amplitude of fluctuation is given by

$$\langle |u_{lm}|^2 \rangle = \frac{r_o^2 k_B T}{\kappa_c (l+2)(l-1)[l(l+1) - \tilde{\gamma}]} \quad , \tag{2.16}$$

where

$$\tilde{\gamma} = \frac{\gamma r_o^2}{\kappa_c} \quad , \tag{2.17}$$

and T is the temperature. The Lagrange multiplier, γ, which accounts for the constraint of constant excess area, physically corresponds to a lateral tension arising from the higher modes requiring more excess area than the lower modes. κ_c is the bending elastic modulus and it is this quantity that determines the "stiffness" of the bilayer.

Because the modes are overdamped (Brochard and Lennon, 1975), the angular frequency of each mode is actually an imaginary frequency. This decay rate is given by

$$\omega_l = \frac{\kappa_c}{\eta r_o^3} (l(l+1) - \tilde{\gamma})/Z_l \quad , \tag{2.18}$$

where

$$Z_l = \frac{(2l+1)(2l^2+2l-1)}{l(l+1)(l+2)(l-1)} \quad , \tag{2.19}$$

and η is the viscosity of the fluid. In the limit of a stiff membrane, the lowest energy mode is forced to accept the excess area and this mode will develop a large amplitude and hence the droplet will become an ellipsoid, as discussed by Peterson (1988).

Using microscope techniques to observe giant Di-myristol Phosphatidylcholine vesicles ($r_o = 9.91\mu$m), the lowest order mode was found to have an amplitude of $\sim 1\mu$m and a corresponding relaxation time of 2.55 seconds, (Duwe et al., 1990). By scaling these results for large vesicles, in which $r \sim 50$nm, the amplitude scales as r and the relaxation time scales as r^3, and therefore, an amplitude of 5 nm with a corresponding relaxation time of ~ 320 ns is expected.

Chapter 3

Experimental Details

Two types of light scattering experiments, static light scattering and dynamic light scattering, were performed to investigate the size and shape fluctuations of vesicles. This chapter contains descriptions of the light scattering apparatus and equipment set-up, the vesicle suspension preparation and the general experimental procedure that was followed.

3.1 Equipment Set-up

The light scattering set-up used for both dynamic and static measurements was built by ALV of Langen, Germany. It consists of a laser, alignment optics, a temperature-controlled scattering chamber, detection optics including a photomultiplier tube, and a correlator. The mounting of the detection optics on a motorized control allows light scattering measurements to made at a range of scattering angles. Alignment of the incident laser beam and the detection optics is such that for each possible scattering angle, the centre of the scattering volume coincides with the center of the scattering cell. The optics are enclosed to minimize the effect of stray light. To isolate the experiment from external noise and vibration, the entire set-up is mounted on a floating Melles Griot optical table.

3.1.1 From Source to Detection

A schematic of the apparatus is shown in Fig. 3.1. The incident light from a 35 mW helium-neon laser, Spectra-Physics Model 127, has a wavelength of $\lambda = 632.8$ nm that is initially horizontally polarized. In the path of the beam between the laser and the scattering

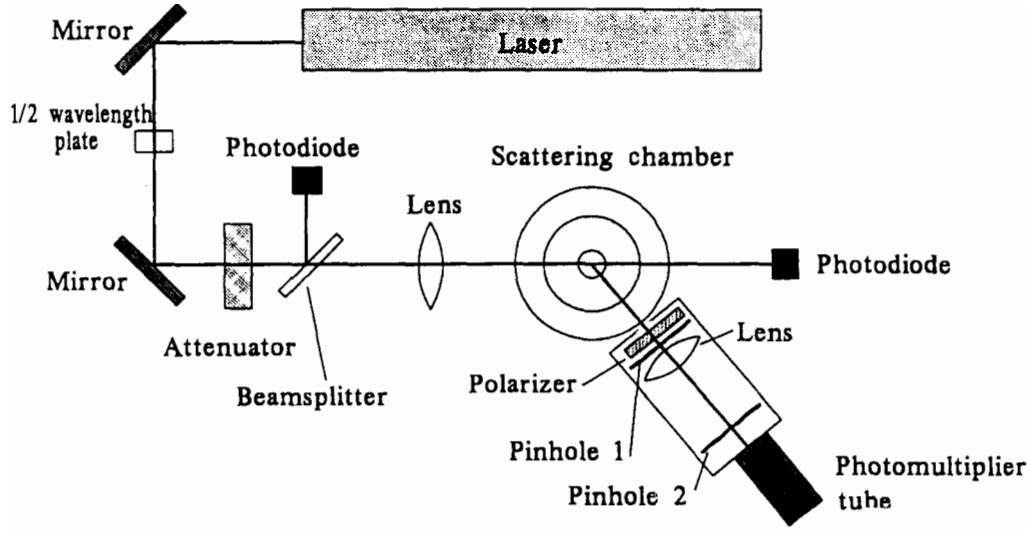

Figure 3.1: Top view of experimental set-up

chamber are two reflecting mirrors, a half-wavelength plate, an attenuator, and a focusing lens: the relecting mirrors simply direct the incident beam through the center of the sample volume. The half-wavelength plate rotates the polarization of the light by 90° to a vertical polarization. The beam then passes through an attenuator which may be used to adjust the intensity of the beam to keep the scattered light to levels safe for the photomultiplier tube. A beamsplitter is used to direct a small part of the incident beam to a photodiode which monitors the incident intensity, a second photodiode also monitors the transmitted intensity. And finally, the lens focuses the beam onto the centre of the scattering cell.

The scattering chamber is shown in detail in Fig. 3.2. It is of cylindrical symmetry and consists of a quartz vat filled with fluid in which sits the glass ampule containing the sample. The fluid, usually toluene, typically has an index of refraction comparable to the scattering cell and is used both to regulate temperature and to reduce reflections and stray light at the fluid/sample cell interface. The ampule is also of cylindrical symmetry and is accurately located on the optical axis of the apparatus by the use of a collet, which may be tightened to secure the ampule. The vat has an entry window for the entrance beam and an exit window for the transmitted beam which is also parallel to the optical axis. It is housed in a hollow casing constructed to allow the incident and transmitted beam to enter and exit

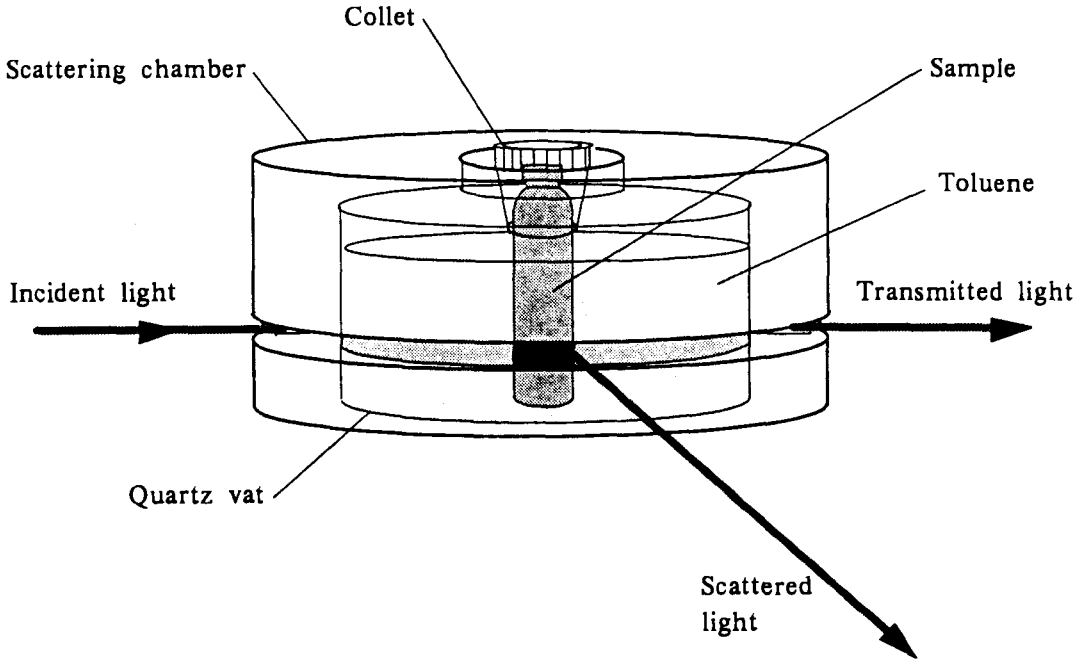

Figure 3.2: This is the scattering chamber

the chamber. The casing encloses the entire vat except for a thin half-circle slice from which the scattered light can be detected through the glass walls of the vat and for the opening in the top through which the sample ampule can be inserted and removed. Water from a Neslab RTE-100 Refrigerated Bath/Circulator is pumped through the hollow casing to act as a thermostatic control, with a temperature range from $-15°C$ to $+130°C$ with stability $\pm 0.01°C$. A platinum resistance thermometer in the toluene measures the temperature and this is taken to be the temperature of the sample.

In the single scattering regime, in which there is a low probability of scattering, most of the light is transmitted. However, the light that is scattered by the particles is scattered in all directions. In the plane of the detection optics, the cylindrical symmetry of the vat leads to the low angular deviation of the detected light, although there is always some reflection of the light at each interface.

While the detection optics are mounted on a motorized platform or goniometer, the range of possible scattering angles is $16° \leq \theta \leq 150°$ and does not extend to a wider range

of angles due to both stray light problems from the incident and transmitted beams, and mechanical obstruction. The detection optics of the scattered light consists of two pinholes, an optional polarizer, one lens, and a photomultiplier tube. Each pinhole is 400 μm in diameter. The first pinhole is the entrance pupil and defines Δq, the range of the scattering wavevector, while the second pinhole is the exit window and defines the width of the beam as "seen" by the photomultiplier. The lens, which sits between the pinholes, images the sample volume onto the surface of the photomultipler. The signal from the photomultiplier tube is sent to the ALV-Correlator mounted in a Zenith 386 PC.

3.1.2 Photomultiplier

The scattered light falls on the photomultiplier where each photon is amplified to produce a current pulse. The total number of pulses $\bar{n}$ in a time Δt is given by

$$\bar{n} = I(t)Q\Delta t \quad , \tag{3.1}$$

where $I(t)$ is the intensity defined as the number of photons hitting the area of the photocathode per unit time, and Q is the quantum efficiency of the photomultiplier. Current pulses are counted in a digital correlator, and a correlation function is calculated. Since the number of counts in a time Δt is proportional to the total intensity $I(t)$, the photon count correlation is equivalent to an intensity correlation.

3.1.3 Correlator

The basic algorithm for a digital photon count correlator is as follows: input pulses are first counted for a sample time δt and then stored. The current count is multiplied by a delayed count, which had been counted some time $\tau = k\delta t$ previously, where k is an integer, and this time is called a lag time. Then, this is followed by a summation of the products. The storing of the count, the multiplication and the summation steps are performed for several channels or lag times in parallel. From the algorithm, the measured correlation function is thus

$$G_2(\tau) = \sum_{j=0}^{N-1} n_j n_{j+k} \quad . \tag{3.2}$$

The apparatus used here incorporates the ALV-5000 Multiple Tau Digital Correlator. This correlator has lag times that are a logarithmically spaced series, as obtained by increasing the original by powers of two, to provide a much larger range of detection for long

decay times. With 35 different sample times ranging from 0.2 μs to just under 4 minutes, a range of lag times from 0.2 μs up to several hours can be sampled.

Another characteristic of this correlator is that it performs a real-time computation of the photon correlation function. At times less than 3 ms, the calculation is performed in hardware with 8×8 bit processing for maximum speed. At these lag times, truncation errors are neglible since the number of counts is small and so the numbers to "carried over" are small. Each time the sample time is doubled, the computational load is decreased by a factor of two and so eventually the computation can be continued in software. At times above 3 ms, the calculation is performed in software with 16×16 bit processing, since speed of calulation is not so crucial but the increased accuracy is needed.

The other function of the correlator is to normalize the correlation function. The correlator has two sets of monitors, "direct" and "delayed". The "direct" monitor records the exact sum of counts for each of the 35 *sample times*. The "delayed" monitor records the sum of counts processed for each *lag time* above the 16th channel. In the symmetric normalization scheme, the normalized correlation function $g_2(\tau)$ is calculated to be

$$g_2(\tau) = \frac{G_2(\tau)}{n_o n_\tau} \quad , \tag{3.3}$$

where $G_2(\tau)$ is the raw correlation function, n_o is the sample-averaged count from the direct monitor and n_τ is the sample-averaged count from the delayed monitor. This form of normalization significantly decreases the relative noise at large lag times over a normalization form with only a single set of monitors (Ruf, 1987).

3.2 Sample Preparation

Three different types of vesicles were tested for their suitability: spontaneous surfactant vesicles, pH-jump vesicles, and extruded phospholipid vesicles. Surfactant vesicles were produced following the method of Kaler (1992) using the surfactants cetyl trimethylammonium tosylate (CTAT) and sodium dodecylbenzenesulphonate (SDBS). These so-called spontaneous vesicles form upon the dispersion of dry anionic and cationic surfactant into water. It is believed that the anionic and cationic surfactants combine into pairs to form wedge shapes and that these wedge shapes can fit together with some sort of natural curvature. Hence, by varying the relative amounts of surfactant, different vesicle sizes could then be accessed. The attraction of this method is in the ease with which various sizes of

vesicles can be made and that these vesicles should be a thermodynamically stable phase. However, while some of the mean vesicle sizes obtained were larger than for the extruded vesicles, the spontaneous vesicles were found to not only be very polydisperse but also to have multimodal distributions.

Following the procedure of Li and Haines (1986), pH-jump or pH adjustment vesicles were made. This method consists of dissolving an anionic lipid di-oleoyl phosphatidyl-ethanolamine (DOPE) in a KCl salt solution, adjusting the pH (raising it to about pH 10.65) and then rapidly lowering it to the original pH (pH 8.6). It is believed that balance between the attractive vs. repulsive interactions of the inner monolayer results in a spontaneous curvature. These vesicles ($r \sim 200\ nm$) were found to vary from batch to batch with different sizes and degrees of polydispersity. Although the distributions were unimodal, they were wider than those obtained for the extruded vesicles.

The technique of extrusion involves the use of pressure to push the phospholipid suspension through double polycarbonate membranes. Extruded vesicles, in comparison to those produced by other methods, are more monodisperse and can be made fairly consistently (Olson et al., 1979). Through freeze-fracture electron-micrographs, it has been found that 100 nm pore-size filters produce 100 nm diameter unilamellar vesicles with a relatively narrow size distribution, while increasing the pore size increases not only the average size but also the distribution of sizes and the occurrence of multilamellar vesicles. The size distribution has also been found to vary with the number of extrusion passes, with the greatest difference occurring in the first two passes, by the tenth pass, the extrusion process seems to have very little effect on the distribution of the suspension. It is believed that those vesicles smaller than the filter pore size will, once formed, pass unaltered through the filters (Clerc and Thompson, 1994).

The phospholipids used were Di-elaidoyl Phosphatidylcholine (DEPC) and Di-myristoyl Phosphatidylcholine (DMPC) purchased from Avanti Polar Lipids. Although both these phospholipids have the same headgroup regions, their tails differ in the number of carbon atoms. In each tail, DMPC has 14 carbons and no double bonds while DEPC, depicted in Fig. 3.3, has 18 carbons with a trans-bond, which is the more stable double bond configuration.

Dry phospholipid was dispersed into the appropriate solution — de-ionized water, NaCl solution, or glycerol solution — to a concentration of 1 mg/ml of lipid. Once hydrated, the lipids spontaneously assemble to form closed multilamellar structures of varying shapes

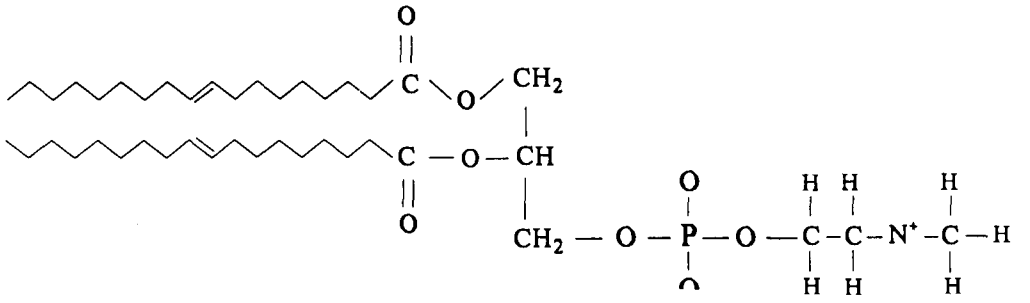

Figure 3.3: Chemical Structure of phospholipid DEPC. A phospholipid consists of a hydrophilic head region connected by a phosphate group and a glycerol molecule to the two hydrophobic carbon chains in the hydrophobic region of the tail.

with sizes of 5-10 μm.

The phospholipid suspension was then subjected to a freeze-thaw procedure, which is found to produce more vesicles of unilamellar character rather than of multilamellar character (Hope et al., 1985). This procedure consists of 5 freeze-thaw cycles with each cycle consisting of the following steps: 5 minutes of immersion in liquid nitrogen to freeze the suspension, followed by approximately 5 minutes in a heated bath set at $\sim$ 40°C to thaw the suspension, followed by approximately 5 minutes of vortexing (i.e. shaking) to mix the suspension. Ice formation during freezing is believed to disrupt the multilayers and promote solute equilibrium.

The vesicle suspension was then pressure filtered or *extruded* through two stacked Nucleopore membrane filters using the Lipex Extruder, as schematically shown in Fig. 3.4. The extruder has 10 mL capacity and is constructed so as to allow temperature control of an extrusion using a water bath. Extrusion of the suspension was performed at 400 psi and at 25°C for DEPC phospholipid and 40°C for DMPC phospholipid. After 10 successive passes through the Extruder, the suspension was diluted to the desired concentration with the appropriate filtered solution. The pore size of the membrane filter used was either 100 nm or 200 nm, depending on the size and distribution of vesicles desired.

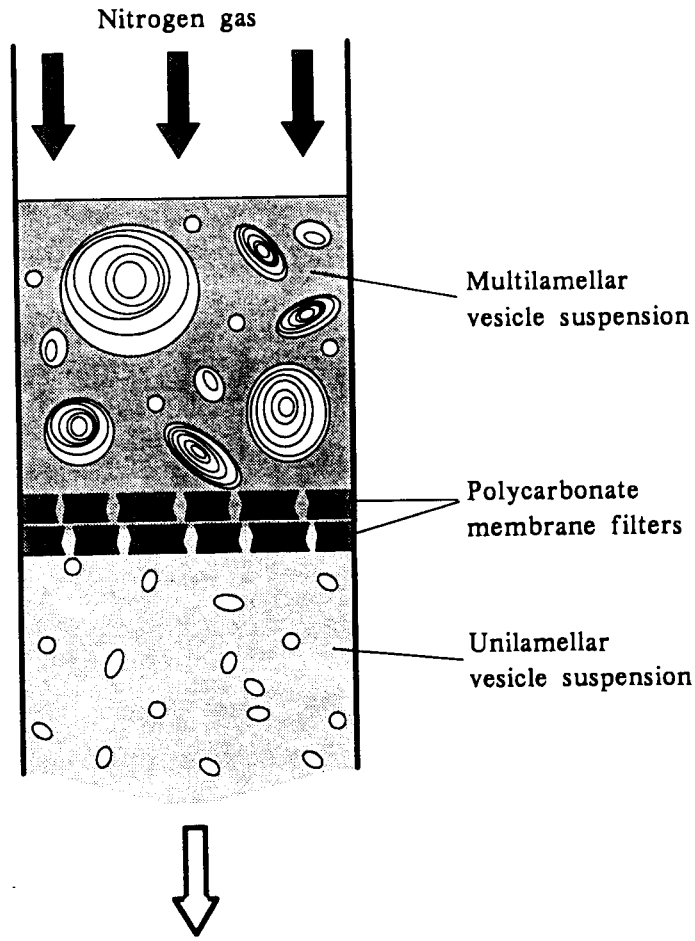

Figure 3.4: Multilamellar structures are pushed through the filters to become unilamellar vesicles

3.3 Experimental Procedure

The sample is made via the steps in Section 3.2. Since dust in the sample is a serious problem, great care is taken to avoid contaminating the sample with dust and most of the preparation work is carried out in a laminar flowhood. Dust that is much larger than the particles of interest scatters a great deal of light and will distort the baseline of the correlation function. Dust that is about the same size as the sample particles may lead to false conclusions about the dynamics of the particles. Samples with obvious dust contamination, as observed in the count rate or in the shape of the correlation function, are filtered or re-extruded or discarded. However, dust that is particle-sized could not be filtered out. The suspension is diluted to a final concentration such that the particles are 100 particle lengths apart to minimize multiple scattering and interparticle interactions. For phospholipid vesicles at this concentration, the suspension appears marginally cloudier than pure water.

The glass ampule which holds the sample to be measured is checked for scratches and imperfections which may distort the light. Its exterior is also cleaned before insertion into the scattering chamber to avoid contamination of the toluene in the vat. Once the ampule is in place, the transmitted beam is checked to see that the ampule is centered on the beam by using the position of the beam as an indicator, because deviation of the beam is usually caused by an uncentered ampule. The sample is then allowed to equilibriate to the set temperature before measurements begin. Intensity of the beam is adjusted via the attenuator if the sample is strongly scattering to keep the count rate at levels safe for the photomultiplier.

For dynamic light scattering, the expression

$$\frac{\Delta\Gamma}{\Gamma} = 4\sqrt{\frac{1}{\Gamma t}} \sim 0.5\% \text{ or } 1\% \quad , \tag{3.4}$$

as discussed in Degiorgio and Lastovka (1971), was used as a guideline to set the measurement time t, where Γ is the characteristic decay rate of the sample for the particular scattering angle. Note that the measurement time required for the same precision is longer for a slow decay rate (large lag time τ) than it is for a fast decay rate. However, if the count rate is too low, there will be noise in the fast channels due to the small number of accumulated counts therein and the total measuring time t must be increased.

The polarizer, located among the detection optics, transmits only light of a particular

polarization while light otherwise polarized is blocked with a 99% efficiency. For the following experiments, since the incident light is vertically polarized, the main component of scattered light is similarly polarized, while the other scattered components are considered to be *depolarized*. The polarizer, set to transmit mainly horizontally polarized light, was used to increase the signal of depolarized scattering relative to the main component of the scattered light, since rotational diffusion and fluctuations are believed to result in a depolarized signal.

Chapter 4

Methods of Analysis and Polydispersity

The time dependent intensity-intensity correlation function $g_2(\tau)$ was computed by the ALV-5000 correlator for light scattered from a suspension of vesicles. Various curve fits were then attempted to determine the number and the values of individual decay rates. While an exponential decay is expected from the translational diffusion of the vesicles, the presence of a second decay time may indicate the presence of shape fluctuations. Should the fluctuations have such a small amplitude that a second decay time is not determined, systematic deviations of the exponential decay at short τ will indicate them indirectly. The difficulty of fitting the correlation function is further complicated by the problem of polydispersity, meaning that the sample is not monodisperse but has a distribution of particle sizes. This polydispersity influences the shape of the correlation function $g_2(\tau)$ and the scattered intensity $I(q)$.

In this chapter, the form of the data is discussed, as are the fitting procedures. The remainder of the chapter is an analysis of the effects of polydispersity on modelled data.

4.1 Analysis

Although the measured quantity is the intensity-intensity correlation,

$$g_2(\tau) \equiv \langle |E_s(0)E_s(\tau)|^2 \rangle \quad , \tag{4.1}$$

the quantity that is calculated through theory is the field-field correlation function,

$$g_1(\tau) \equiv \langle E_s^*(0) E_s(\tau) \rangle \quad . \tag{4.2}$$

How are the two related? As a result of the many particles in the scattering volume and their independence, the total scattered field is considered to be a sum of independent random variables. The Central Limit Theorem then implies that the scattered field, which itself is a random variable, must be distributed according to a Gaussian distribution. Because such a distribution is completely characterized by its first and second moments, its higher moments can be written in terms of the first two:

$$g_2(\tau) = |g_1(0)|^2 + |g_1(\tau)|^2 \quad , \tag{4.3}$$

where $|g_1(0)|^2$ is the dc component or the *baseline*. This is more commonly written as the Siegert relation,

$$g_2(\tau) = 1 + \beta |g_1(\tau)|^2 \quad , \tag{4.4}$$

in which β is a geometrical factor of the experimental setup. Because this relation is valid when the number fluctuation of the particles in and out of the scattering volume is small, as explained above, deviations will be on the order of $1/N$, where N is the number of particles in the scattering volume.

A typical normalized intensity-intensity correlation function obtained from experiment is shown in Fig. 4.1. The general shape of the function is exponential but not single exponential — its initial slope is called the *decay rate*, its asymptotic value is referred to as the *baseline*, and its y-intercept is the *amplitude* of the decay. As discussed in Section 2.2, the correlation function for a sample of diffusing identical particles should be a single exponential. That this is not the case, is a signal that the vesicles are polydisperse and perhaps are also exhibiting more than one type of motion, i.e. other than translational diffusion, since both have the effect of distorting the exponential.

Because of the polydispersity, there will be contributions to the correlation function from the entire distribution. Particles larger and smaller than the average size will have contributions slower and faster than that of the average size. A "smearing" effect will be produced and this will increase with increasing polydispersity; and so the resulting correlation function will have the shape of a distorted exponential.

A second time scale may similarly result in a distorted exponential for the correlation function. Two types of motion of the vesicles could be the cause of this additional time

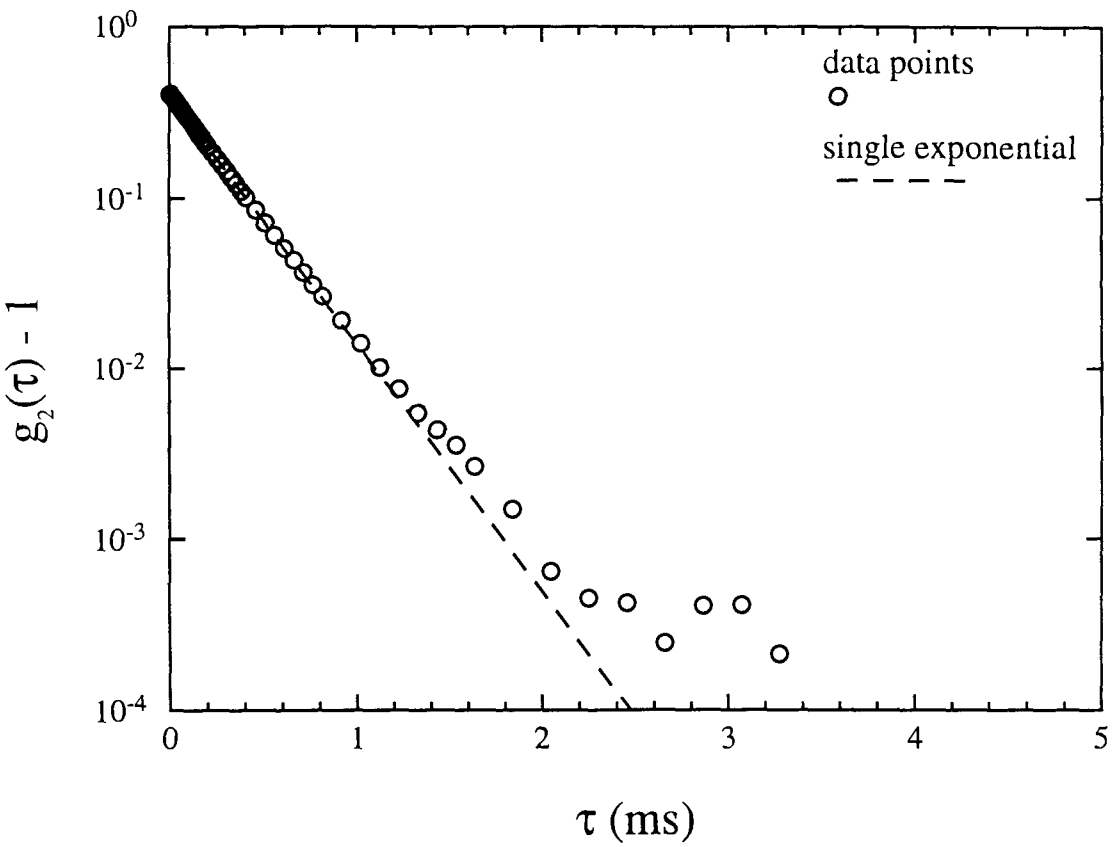

Figure 4.1: Typical correlation function measured using DLS from a sample of extruded vesicles. The initial slope is the mean decay rate, the y-intercept is the amplitude, and the asymptotic value is the baseline. These were DEPC vesicles extruded through 100 nm pore size filters, measured at a scattering angle of 90° and at a temperature of 25°C. As a comparison, the dotted line represents a single exponential decay.

scale: shape fluctuation and rotational diffusion. Vesicles fluctuating in shape will have a time scale on the order of 10 kHz to 10 MHz associated with their fluctuation, as discussed in Section 2.3. It is likely that the shape fluctuation's amplitude relative to that of the translational diffusion is quite small and so while a second decay is not obvious, the effect of the fluctuation could be a distortion of the correlation function away from a single exponential. Alternatively, the additional time scale could be associated with the rotational diffusion of an ellipsoidal vesicle; depending upon the stiffness of the bilayer, the time-averaged vesicle shape may be spherical (in the floppy limit) or it may be ellipsoidal (in the stiff limit). Although the time scale for rotation is supposedly much closer to that of translation than that for the shape fluctuations, it is unclear that the effects are independent. A collection of vesicles fluctuating from one ellipse to another may very well appear as a collection of rotating ellipses.

So then the task is to analyse the correlation function to quantify the polydispersity of the vesicles and to distinguish the presence of additional time scales. By writing the field-field correlation function as an integral of correlation functions averaged over the distribution of decay rates $w(\Gamma)$, it can be recognized as the Laplace transform of $w(\Gamma)$,

$$g_1(\tau) = \int_0^\infty w(\Gamma) e^{-\Gamma\tau}\, d\Gamma \quad , \tag{4.5}$$

assuming positive decay rates. To find the distribution of decay rates, the correlation function must be inverted to obtain $w(\Gamma)$. Because it is impossible to measure the range of $\Gamma = 0$ to ∞, only an approximation to the inverse may be found. In practice, the result is an entire set of solutions that exist to within experimental error, however, the members of this solution set can also be very different from one another. Such mathematical problems are classified as being ill-conditioned and the challenge is to find the most probable solution from all of the possible solutions.

The analysis methods used to deal with the difficulty of the Laplace transform can involve limiting the amount of information obtained, incorporating some *a priori* information, regularization methods or some combination thereof. By assuming a specific analytic form, with such forms as a single or double exponential, the ill-conditioned nature is essentially removed and the data can be fit using a non-linear least squares fit program. For roughly exponential decays, the method of cumulants is an expansion of the distribution about its moments, and is useful for obtaining an average decay rate and an indication of the width of the distribution about this average. A double exponential functional form is used

when fitting a bimodal distribution of decay rates. If the form of the distribution is not known, CONTIN, a general Laplace inverse transform package incorporating regularization (i.e. smoothing) is useful as a qualitative probe for determining the number and relative magnititude of decay rates.

4.1.1 Non-linear Least Squares Fit

For both the analytic forms of the cumulant expansion and the double exponential function, the C program nnlsq-Nonlinear Least Squares Fit written by A. Kornblit, was used to fit the data. In the nnlsq program, a given set of N data points is fitted to a given model function with adjustable parameters. The sum of the squares of the residuals, the so-called merit function,

$$\chi^2 = \sum_{i=1}^{N} \left[\frac{(y_i - y_i^{fit})}{\sigma_i} \right]^2 \tag{4.6}$$

is an indication of the goodness of the fit, where y_i is the ith data point, y_{fit} is the ith fit point, and σ_i is the weighting factor of the ith data point. The merit function is minimized with respect to all model parameters a_j to find the maximum-likelihood of the fitted parameters, such that the matrix of derivatives vanish:

$$\frac{\partial \chi^2}{\partial a_j} = 0 \quad . \tag{4.7}$$

Since the dependence of the model function on its parameters is non-linear, a closed form cannot be found, and an iterative procedure must be used to find the solution. A correction vector towards the absolute minimum of the χ^2 surface in parameter space is calculated from the given initial trial parameter values. A new correction vector is then calculated from the adjusted parameters and the process is continued until convergence is reached, where the correction vector is less than some preset value.

The Marquardt algorithm that is used to search for the minimum in this program is actually a combination of two common algorithms, the Taylor expansion method and the Gradient method. The former is suitable in the vicinity of the minimum, where the function is expanded as a local quadratic surface about the minimum, while the latter is useful for rapid convergence far from the minimum. The Marquardt algorithm combines the advantages of both methods by varying smoothly between the two until convergence is reached. For further details, refer to Press (1992).

Cumulant Expansion

The method of cumulants to extract information from the field correlation function was first discussed by Koppel (1972). Cumulant expansion has become widely used due to its applicability to many systems, its low number of parameters, and its good convergence and stability of the fitted parameters. The cumulant expansion is defined by setting

$$\ln g_1(\Gamma,\tau) = \sum_{n=1}^{\infty} \frac{(-\tau)^n}{n!}\mu_n(\Gamma) \quad , \tag{4.8}$$

where μ_n is the nth cumulant. If the field correlation function can be written in the form of a weighted set of exponentials, as in Eq. 4.5, then the first three terms of the expansion are related to the moments of the distribution,

$$\begin{aligned} \mu_1(\Gamma) &= \langle\Gamma\rangle \\ \mu_2(\Gamma) &= \langle\Gamma^2\rangle - \langle\Gamma\rangle^2 \\ \mu_3(\Gamma) &= \langle\Gamma^3\rangle - 3\langle\Gamma\rangle\langle\Gamma^2\rangle + 2\langle\Gamma\rangle^3 \quad . \end{aligned} \tag{4.9}$$

$\langle\Gamma^m\rangle$ are the moments of the distribution, defined such that

$$\langle\Gamma^m\rangle = \int dx\, \Gamma^m w(x) \quad . \tag{4.10}$$

While the probability distribution is completely specified if all the moments are known, the expansion can be truncated if the higher moments are small. The mean value of the distribution is the initial slope of the decay and is given by the first cumulant. The second cumulant is the variance of the distribution and thus the dimensionless ratio, μ_2/Γ^2 gives an estimate of the dispersion about the mean value and an indication of the polydispersity of the distribution. For convergence reasons, such an expansion is valid for small τ and narrow $w(\Gamma)$ for which (empirically)

$$\frac{\mu_2}{\Gamma^2} \leq 0.3 \quad . \tag{4.11}$$

The model function that was fitted using the nnlsq routine was

$$g_2(\tau) = B + Ae^{-2\bar{\Gamma}\tau+\mu_2\tau^2} \quad , \tag{4.12}$$

where B is the baseline, A is the amplitude, $\bar{\Gamma}$ is the average decay time, and μ_2 is the second cumulant. Higher order terms were not necessary.

Double Exponential Function

The double exponential function is used to fit a bimodal distribution of Γ, which may arise from the scattering due to the translation and shape fluctuation or to the translation and rotation of vesicles. The model function that is used in the fit is

$$g_2(\tau) = \left(A_1 e^{-\Gamma_1 \tau} + A_2 e^{-\Gamma_2 \tau}\right)^2 + B \quad , \tag{4.13}$$

where A_1, Γ_1 are the amplitude and the decay rate of one time scale and A_2, Γ_2 are associated with the second time scale, B is the baseline. In looking for rotation or fluctuation of the vesicles, the data over a range of q was first fitted with the cumulant fit to find the most likely value of the diffusion coefficient and the corresponding decay rate. The data was then re-fitted using the double exponential function using this mean decay rate as a fixed parameter while allowing the other parameters to float. Once fitted, random residuals and a consistent second non-zero amplitude and characteristic decay time are an indication of other dynamics such as rotation or fluctuation.

4.1.2 General Laplace Transform Inversion

The program Contin was developed by Provencher (1982a,b) to invert noisy linear integral equations without having to specify an analytic form. An optimal solution is found by searching for the simplest solution consistent with *a priori* knowledge and experimental data. The merit function is the sum of a least squares quadratic term with a quadratic constraint term,

$$\chi^2 = A^2 + \lambda B^2 \tag{4.14}$$

Consider the merit function as the sum of two terms, A^2 and λB^2. Term A^2 is an indication of the agreement of the model with the data and is the same expression as for the merit function of the non-linear least squares fit as discussed above. By minimizing a merit function of A^2 alone, the resulting solution will have good agreement with the data but may be unstable, physically impossible, or oscillating. In contrast, the second term is a measure of the smoothness of the fit, although minimizing it alone results in solutions that are stable and smooth, these may have very little relation to the actual data. As used by CONTIN, the constraint term is calculated from the second derivative of the distribution. The strength of the regularization/smoothness is controlled by λ, which is a positive number. The merit

function is calculated for a specified number of λ and the most probable value using the statistical Fisher F-test is chosen such that λ is at its largest value consistent with the available data. For further details as to the actual fitting routine, refer to Provencher (1982a,b).

As implemented by the ALV-5000 board, Contin fits to the field correlation function $g_1(\tau)$. The Siegert relation, Eq. 4.4, is used to transform the intensity-intensity correlation $g_2(\tau)$ of the experimental data, to the field-field correlation. Unfortunately, with the procedure of taking the square root, the noise level at large lag times is increased and any negative noise may result in extra spurious, shifted or broadened peaks when analysed.

The main advantage of using CONTIN is that stable and smooth solutions can be found without knowing very much about the dynamics of the sample. For our purposes, it was used mainly as a qualitative tool to identify multimodes, for example, rather than as a quantitative method of analysis.

4.2 Polydispersity Calculations

To better understand the polydispersity of the vesicle sample and its effect on the data obtained from light scattering experiments, results with a known distribution and polydispersity were calculated. By comparing the values obtained from analysing these calculated results with the parameters used in its creation, the analysis methods can be tested and calibrated. Simulated results are also a good way to determine the effect of the polydispersity.

4.2.1 The Schulz Distribution

The two parameter unimodal Schulz distribution (Aragon and Pecora, 1976) shown in Fig. 4.2 was used to model this polydisperse system. The normalized distribution of particles having a radius ratio $z = r/\bar{r}$ is

$$N(z) = \frac{1}{m!}\frac{(m+1)^{m+1}}{\bar{r}} z^m e^{-(m+1)z} \quad , \tag{4.15}$$

where $\bar{r}$ is the number-average radius of the particles, and $m = 0, 1, 2, \ldots$ is a measure of the sharpness of the distribution. The common measure of the width of the distribution, the standard deviation σ, is related to the parameter m such that

$$\frac{\sigma}{\bar{r}} = \frac{1}{\sqrt{m+1}} \quad . \tag{4.16}$$

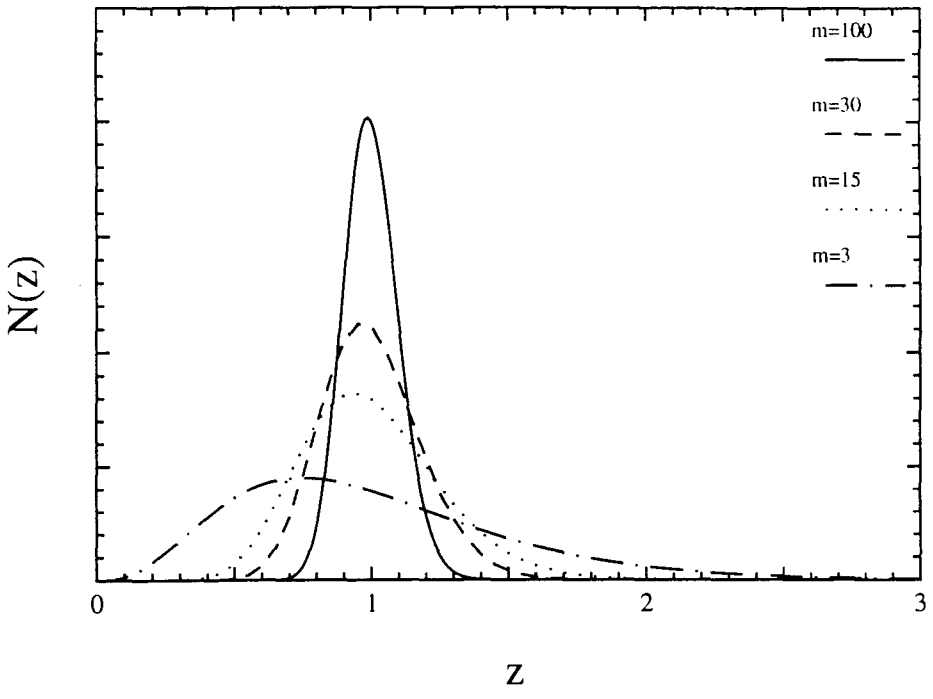

Figure 4.2: The Schulz distribution was used to model the polydisperse vesicle sample where z is the fractional size and m is the polydispersity parameter. The smaller the m value, the higher the polydispersity, and the more skewed is the distribution. The distribution is normalized such that the area under the curve is equal to one.

Thus, the smaller the value of m, the wider and the more skewed is the distribution. For large m, the function has an asymptotic approach to a Gaussian shape. Although a Gaussian distribution could also be used, the skew of the function towards the larger sizes of the distribution appears to be especially appropriate for biological systems, which have a tendency to form small quantities of aggregates.

4.2.2 Effect of Polydispersity on Form Factor

Initially, the effect of polydispersity on the form factor was investigated by modelling the vesicles as thin spherical shells, with the same fluid inside and outside. This form factor is the scattering due to the internal structure of the scattering particle. For identical spherical shells of some thickness much smaller than the wavelength of light, the form factor is given

by the square of the asympotic limit of the zeroth-order Bessel function,

$$P(x) = \frac{\sin^2(x)}{x^2} \quad , \tag{4.17}$$

where the dimensionless parameter,

$$x = qr \quad , \tag{4.18}$$

and q is the scattering wavevector and r is the radius of the scattering particle. The scattered intensity consists of this form factor and a mass factor which arises because the polarizability of each particle is proportional to the number or mass of the molecules in the particle. Since the scattering particles are spherical shells, the mass of each scatterer is proportional to the surface area ($\sim r^2$) and not the volume. Because the intensity is proportional to the square of the polarizability, the mass factor has a r^4 dependence. To include the effect of polydispersity, the scattered intensity was integrated over the Schulz distribution via the Numerical Recipes in C routine, qsimp,

$$I_{poly}(x) = \int r^4 P(x) N(z)\, dz \quad . \tag{4.19}$$

As shown in Fig. 4.3, the resulting function with polydispersity is similar in shape to the function without polydispersity but with far less sharp minima. Furthermore, increasingly polydisperse results have shallower minima, and, the distribution in size causes a superposition of form factors according to the size distribution.

4.2.3 Effect of Polydispersity on the Correlation Function

Correlation functions incorporating polydispersity were calculated for different values of m, the polydispersity parameter of the Schulz distribution. The ensemble-averaged correlation function is the integral of a single exponential over the Schulz distribution weighted by the scattered intensity at a given q value,

$$\langle g_1^2(\tau)\rangle = \frac{\int z^4 S(x)\, e^{-D(\bar{r})q^2\tau} N(z) dz}{\int z^4 S(x)\, N(z) dz} \quad , \tag{4.20}$$

where the angular brackets denote a light-scattering ensemble average, D is the diffusion coefficient calculated for the number-average radius, and the denominator is simply a normalization factor.

The form of the results calculated was

$$g_2(\tau) = 1 + \beta\langle g_1^2(\tau)\rangle \pm 0.1\%\,\text{noise} \quad . \tag{4.21}$$

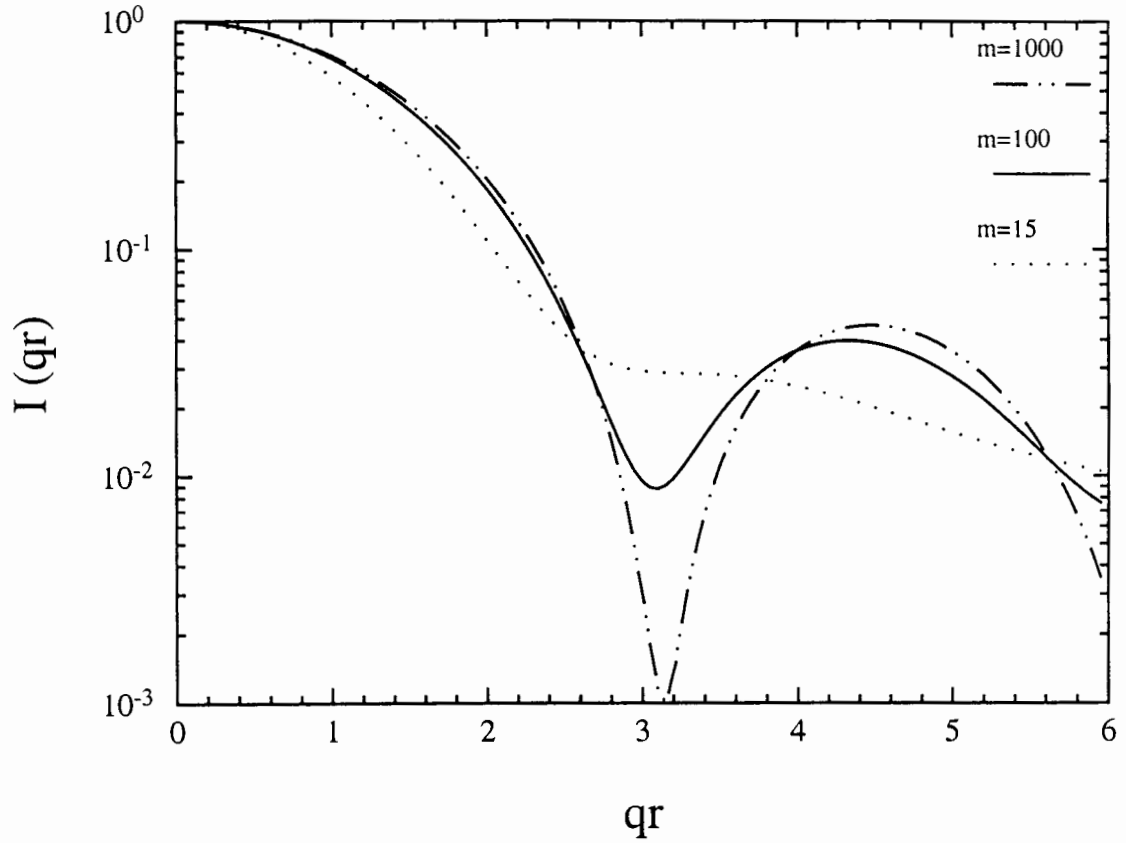

Figure 4.3: Spherical shell scattered intensity for varying degrees of polydispersity as a function of $q\bar{r}$, a dimensionless parameter, where $\bar{r}$ is the number average radius. Note the larger the polydispersity (decreasing m parameter of the Schulz distribution), the more shallow the minima of what was originally (without polydispersity) the zeroth order Bessel function.

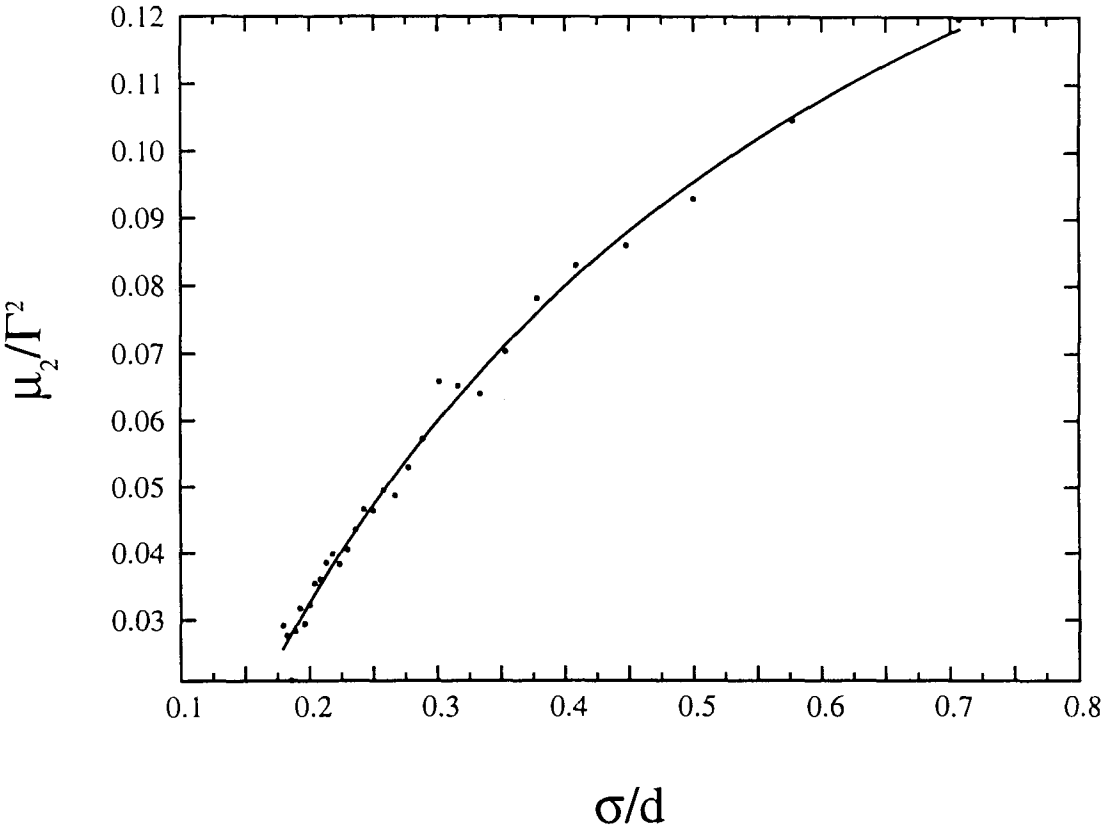

Figure 4.4: Relation of the second cumulant to the standard deviation: the small dots are results of cumulant expansion fits to functions of polydisperse samples calculated using the Schulz distribution, for $\bar{r} = 50$nm, $\theta = 90°$, $m = 0, 1, \ldots, 30$. For the Schulz distribution, the standard deviation is related to the polydispersity parameter m via $\sigma/\bar{r} = 1/\sqrt{1+m}$. The curve is a guide for the eye.

in which β is a factor associated with the geometry of the experimental set-up and was chosen to have the value of 0.4 to agree with the value obtained with our current apparatus. The noise was created by a random number generator initialized in connection with the time clock of the computer. Correlation functions were generated for polydispersity parameters $m = 1, \ldots, 30$ at a scattering angle of $\theta = 90°$. The calculated results were analysed with the cumulant expansion fit and a relation was obtained between the characteristic polydispersity of the sample $\sigma/\bar{d}$, and the standard deviation of the fit, μ_2/Γ^2, as shown in Fig. 4.4. It was found that the higher the polydispersity, the wider the distribution of the fit. By fitting experimental data with the cumulant fit, a value of the polydispersity m of the sample

can then be estimated by the comparison of the experimental and the simulated second cumulant fits. The effect of the polydispersity was a horizontal stretch of the exponential of the correlation function, where again, the size distribution has caused a distribution of the decay times. Results obtained using Gaussian distributions are similar (Aragon and Pecora, 1976).

4.2.4 Effect of Polydispersity on the Diffusion Coefficient

Following the method of Fujime, Takasaki-Ohsita, and Miyamoto (1988), the diffusion coefficient was calculated as function of q, the wavevector. By noting that $\langle D \rangle$ is the first time derivative of $\langle g_1(\tau) \rangle$ and performing an explicit integration [1], the ensemble averaged expression for the diffusion coefficient was found to be

$$\langle D \rangle = \frac{2(m+2)!}{y^2(m+1)^{m+5}} \left[1 - \frac{\cos[(m+3)\tan^{-1}(y)]}{(1+y^2)^{(m+3)/2}} \right] \tag{4.22}$$

where $y = 2q\bar{r}/(m+1)$. Figure 4.5 is a graph of $\langle D \rangle$ vs q and shows the q-dependence of the translational diffusion coefficient for varying degrees of polydispersity. While the translational diffusion of a monodisperse system is q-independent because the particles diffuse at the same rate, the particles of a polydisperse system each diffuse at a rate that is dependent upon their size. Furthermore, since the contribution of scattered light from each particle is dependent upon its size for a given q, larger particles will contribute more at smaller q, while smaller particles will contribute more at larger q. Thus, the diffusion coefficient will be q-dependent for a polydisperse system.

From the relation of the variance of the distribution to the standard deviation, the second cumulant can be expressed as a function of the moments of the diffusion coefficient,

$$\frac{\mu_2}{\bar{\Gamma}^2} = \frac{\langle D^2 \rangle}{\langle D \rangle^2} - 1 \quad , \tag{4.23}$$

where $\langle D \rangle = k_B T/6\pi\eta\bar{r}$ is the Stokes-Einstein relation as discussed in Section 2.2, and $\bar{r}$ is the number-average radius. Shown in Fig. 4.6, the second cumulant of a polydisperse sample is certainly q-dependent, becoming more q dependent as the polydispersity increases.

[1] By use of the integral formula, for $a, \alpha > 0$ and $\alpha \in I$,

$$\int_0^\infty e^{-az} z^{\alpha-1} \cos(bz)\, dz = \frac{\Gamma(\alpha)}{(a^2+b^2)^{\alpha/2}} \cos[\alpha \tan^{-1}(b/a)] \quad .$$

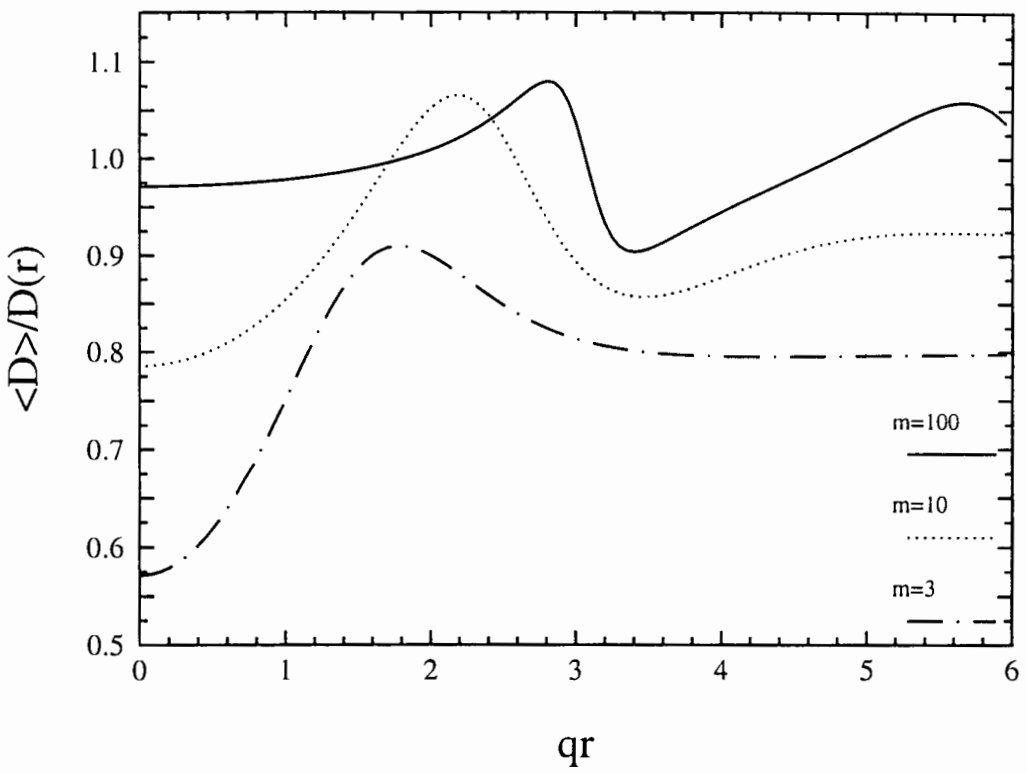

Figure 4.5: The q-dependence of the diffusion coefficient. $D(\bar{r})$ represents the number-average value for the diffusion coefficient. Note that the larger the polydispersity, the greater the deviation from this mean value.

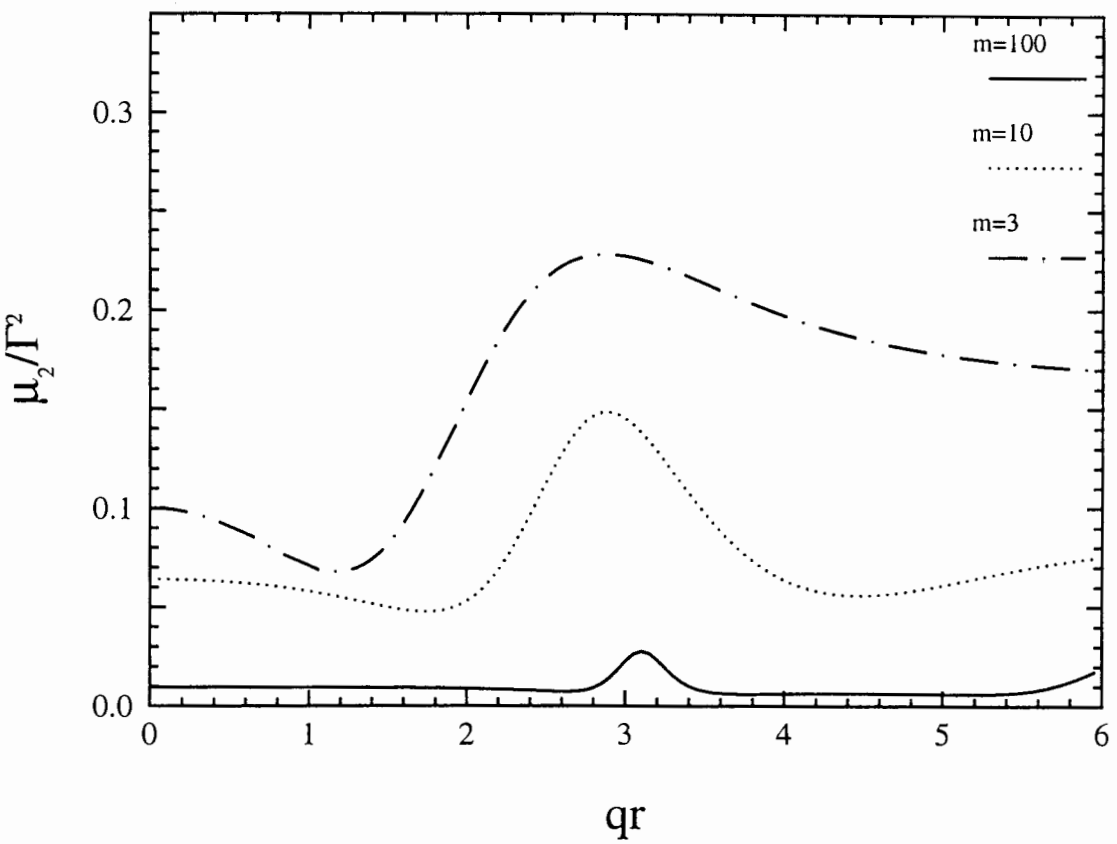

Figure 4.6: The q-dependence of the second cumulant. The larger the polydispersity, the greater the change in the apparent width of the distribution with q.

4.2.5 Polydisperse Ellipsoidal versus Spherical Shells

Because the lowest fluctuation mode is ellipsoidal and such a shape is also the equilibrium shape of a vesicle with small excess area, the scattering from polydisperse ellipsoidal shells was considered. The difference between the scattering from spherical shells and ellipsoidal shells is then an indication of the amplitude of shape fluctuations which should be observable. The axial ratio b/a was chosen to be 1.1 or 0.9 for slightly prolate or slightly oblate, respectively, where b is the major axis and a is the minor axis of the ellipsoid. Using the ellipsoidal shell scattering form factor of Fujime, Takasaki-Ohsita, and Miyamoto, (1988),

$$P_{ellipse}(x) = \int_0^1 \frac{\sin^2[x(1-k\xi^2)^{1/2}]}{x^2(1-k\xi^2)} d\xi \quad , \tag{4.24}$$

where

$$k = 1 - \left(\frac{a}{b}\right)^2 \quad , \tag{4.25}$$

and $\xi = \cos(\theta)$. By integrating over all angles to account for the random orientation of the particles, the ensemble-averaged form factor was calculated. The scattered intensity further incorporating polydispersity was then calculated with Eq. 4.19. Scattering from ellipsoidal shells and spherical shells of equivalent polydispersity and hydrodynamic volume was compared as a function of the scattering wavevector. The percent difference in the structure factor as a function of qr is shown in Fig. 4.7 for varying degrees of polydispersity. The greater the polydispersity, the smaller the difference due to scattering from an ellipsoidal shell and from a spherical shell. In effect, the polydispersity hides the effect of the asymmetry of the ellipsoidal shell and makes it difficult to distinguish between a polydisperse spherical distribution and a polydisperse ellipsoidal distribution.

4.2.6 Summary

In summary, the polydispersity will have two important effects: first it will make both the diffusion coefficient and the standard deviation dependent upon the scattering wavevector and second, it will obscure small amplitude fluctuations.

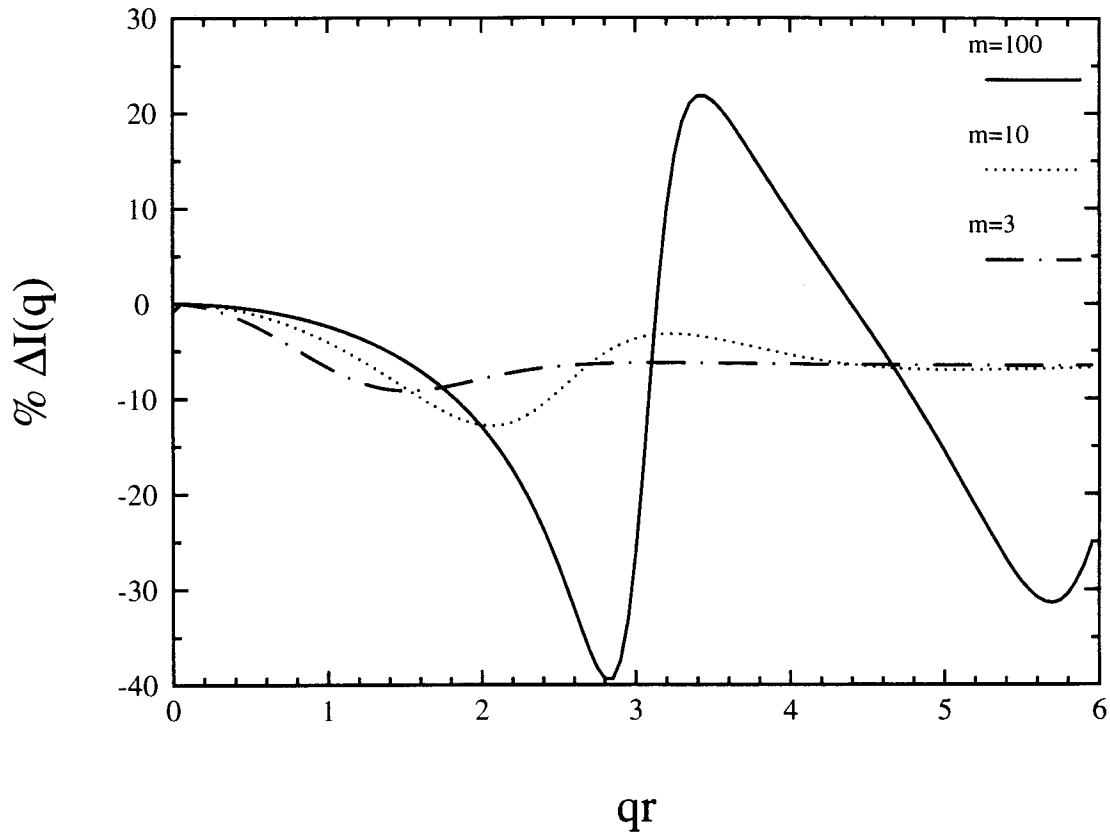

Figure 4.7: The percent scattered intensity difference between a 10% prolate ellipsoidal shell and a spherical shell of equivalent polydispersity and hydrodynamic volume.

Chapter 5

Experimental Results

Light scattering experiments were performed on vesicle suspensions to measure size and shape fluctuations of the vesicles. Because such fluctuations are known to depend on temperature, the viscosity of the suspending fluid, and the excess area of the vesicles, these effects were investigated. First, the effect of temperature on the hydrodynamic radius of DMPC vesicles will be discussed. This will followed by a discussion of the results of increasing the viscosity and then by increasing the excess area for DEPC vesicles.

5.1 Effect of Temperature

The effect of temperature on the mean size of DMPC phospholipid vesicles was investigated using dynamic light scattering. Although increasing the temperature should also increase the amplitude of the shape fluctuations, as discussed in Section 2.3, this is a very small effect. A much larger effect is the increase in the excess area that comes about due to the more rapid thermal expansion of the bilayer relative to the increase in the volume of the vesicle. By enhancing the amplitude of the shape fluctuations to the point where the fluctuations scatter a significant amount of light, we hope to measure the characteristic time scale of the fluctuations. In other experiments based on varying the temperature, such phenomena as budding and increased shape fluctuations have been observed in giant vesicles (H.-G. Döbereiner et al., preprint).

DMPC phospholipid was hydrated in de-ionized water and extruded at 40°C to produce roughly 100 nm vesicles. The temperature was dropped in steps and at each step the measurement was made after the temperature of the sample had stabilized. As the area of

the bilayer is thermally contracted, the fluid inside of the vesicle diffuses out of the vesicle due to mechanical pressure. Water was chosen as the suspending fluid because of the ease with which it crosses the bilayer.

A single exponential decay was measured for the correlation function and found to be consistent with only translational motion of the vesicles. The correlation function was initially fit with a single exponential function but since the fit residuals were systematic and suggested polydispersity, it was then fit with the second cumulant expansion to obtain both an average decay constant and its standard deviation. From this value of the average decay constant, the diffusion coefficient was calculated for the particular wavevector and then used to determine the hydrodynamic radius via the Stokes-Einstein relation, $D = kT/(6\pi\eta r)$, as discussed in Section 2.2. Note that this relation was developed to describe the diffusion of spheres, and as such, the hydrodynamic radius is not necessarily a characteristic length of the diffusing objects, but only a measure of the effective size of the objects as they diffuse and tumble through the fluid.

As shown in Fig. 5.1, the hydrodynamic radius was found to decrease with decreasing temperature. The area per phospholipid headgroup in the bilayer will decrease with decreasing temperature and this results in a contraction of the surface area of the bilayer, and thus, a smaller mean radius of the vesicles. Thermal properties of the bilayer have been studied with sonicated vesicles using both calorimetry and light scattering (Cornell et al., 1981), and with planar bilayers using light scattering (Grabowski and Cowen, 1977). Between 23°C and 24°C, there was what appeared to be a sudden 5% decrease in the hydrodynamic radius. This jump was attributed to the so-called gel transition of DMPC phospholipid: below this transition temperature, the bilayer is in a gel phase in which hydrogen bonds are formed between the hydrocarbon tails of adjacent phospholipids and the phospholipids are "bound". Above the gel transition temperature, the phospholipid molecules are not bound to one another, but are free to translate and rotate within the bilayer plane and, as such, the bilayer is considered to be fluid. It is well known that, as the gel phase is formed, the phospholipids bind closer together, and this results in a sudden decrease in the surface area of the bilayer and hence also the radius of the vesicle. It has been observed that the bending elastic modulus is increased by roughly a factor of three in the gel phase for DMPC planar bilayers (Evans and Needham, 1987). The effective decrease of the surface area due to the formation of the gel phase is larger (over a given temperature range) than that due to the thermal contraction of the bilayer.

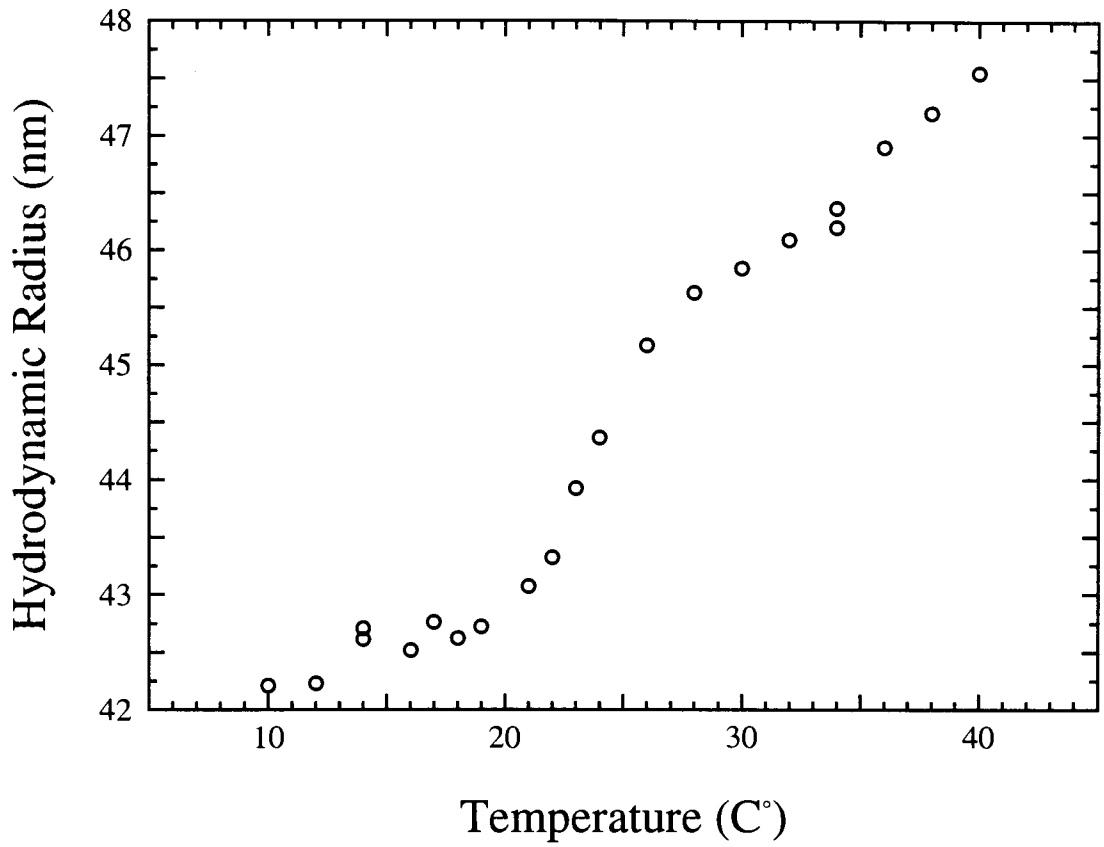

Figure 5.1: Temperature dependence of the hydrodynamic radius of DMPC vesicles in water, as measured at decreasing temperature at a scattering angle of 90°. The sudden change in the radius at $\sim$ 23°C can be attributed to the gel transition of DMPC phospholipid. The error bars are 1% as observed from repeated measurements for the same duration of measurement. μ_2/Γ^2 had an average value of 0.7.

Following the step-wise temperature decrease, the temperature was raised, again in steps, up to the original temperature. The values of the hydrodynamic radius were found to agree with the ones obtained previously and the gel transition was found to be reversible, insofar as the hydrodynamic radius was concerned. Additional measurements were made at the various temperatures for a range of scattering angles, with similar results. Not only was a second time scale not observed, but the standard deviation, which is an indication of the polydispersity and can be expected to increase with an increased amplitude of the fluctuations, appeared to be independent of the temperature.

5.2 Effect of Excess Area

The excess area of the vesicle was increased to enhance the amplitude of the fluctuations by decreasing the volume of the vesicle relative to the surface area. This was done by creating an osmotic pressure difference between the interior and the exterior fluids of the vesicle and exploiting the permeability properties of the bilayer. The permeability of the bilayer, which is a measure of the speed with which a particular substance can diffuse across its width, is such that the bilayer is readily permeable to water, but far less permeable to salt ions. Water, for example, having a permeability coefficient for planar egg-phosphatidylcholine of roughly 10^{+3}cm/s (Deamer and Bramhall, 1986), will diffuse the width of the bilayer in approximately 1 μs. Under similar conditions, sodium and chlorine ions, common salt ions, will diffuse respectively 10^{10} and 10^{7} times slower than water though the bilayer[1]. Thus, by engineering a differential salt concentration between the interior and exterior of the vesicles, the salt ions should remain on their respective sides of the bilayer during the time frame of our experiments and water will pass through the bilayer to equalize the osmotic pressure.

The vesicles were prepared in the following manner: the hydrated DEPC phospholipid suspension was extruded in a particular salt solution and then the exterior salt concentration was altered through dilution with a salt solution of an even higher concentration. Water then leaves the vesicle to make the salt concentration of the interior of the vesicle essentially equal to the exterior salt concentration. Because we assume that the surface area of the vesicle is conserved, then as the volume of the vesicle decreases, a certain amount of excess surface area is created. In principle, since the excess area is the area available for fluctuations, this

[1]Other ions are also used for this purpose. For example, Cullis et al. (private communication) at UBC have used Na_2SO_4 because the sulphate group of the salt diffuses through the bilayer at a much slower rate than the chlorine ion.

volume deflation should increase the amplitude of the fluctuations.

An additional complication is the shape of the vesicles upon extrusion. As found from cryo-EM micrographs by Mui et al. (1993), vesicles extruded in some non-zero salt concentration are sausage-shaped or elliptical, and will remain so in order not to create an osmotic pressure difference. Vesicles extruded in pure water or zero salt concentration are initially sausage-shaped but will become spherical in shape a few hours after extrusion. It would seem that the extrusion process produces vesicles of sausage-type shapes, and hence vesicles made in salt concentrations will have an already existing excess area prior to volume deflation. This unknown amount of excess area may complicate the analysis of the volume-deflated vesicles.

Dynamic light scattering measurements were performed on the volume-deflated vesicles by measuring a correlation function at a particular scattering wavevector q value. The measured correlation function had the form of an exponential decay that was dominated by a single time scale and this time scale was consistent with only translational motion of the vesicles. No evidence of a second time scale was observed, i.e. no direct evidence of fluctuations. The analysis was similar to that performed for the experiment where the temperature was varied: the correlation function was fitted with the second cumulant expansion to obtain the standard deviation and the mean decay rate, from which the diffusion coefficient and the hydrodynamic radius were calculated. Measurements were repeated for different scattering wavevectors to obtain curves of the second cumulant and the hydrodynamic radius as a function of the scattering wavevector. These curves were then examined for possible anomalous behaviour.

5.2.1 Zero Percent Excess Area

The hydrodynamic radius as a function of the scattering wavevector was investigated for vesicles extruded in de-ionized water. These vesicles should exhibit neither rotational diffusion nor shape fluctuations due to sphericity. The standard deviation of the decay rate will then correspond to the polydispersity in the size of the extruded vesicles and not the shape.

As shown in Fig. 5.2, the hydrodynamic radius was found to be q-dependent, changing a total of 4% in a roughly linear fashion. The non-zero slope is the result of polydispersity of the sample, as discussed in Section 4.2.4, or at least something that can not be distinguished from the polydispersity. There is an apparent increase in the magnitude of the slope at both the higher and lower values of the scattering wavevector: the anomalous increase of the

magnitude of the slope at high q may be due to the presence of smaller vesicles. A possible explanation for the increased slope at low values of q is the presence of larger objects in the scattering volume, either dust or aggregates of vesicles. Although dust contamination was minimized with the thorough cleaning of glassware and careful sample preparation under a laminar flowhood, some samples were found to have high levels of dust, and these were discarded. Because of the relatively small amplitude of scattering from these larger objects, which is not much more than from the vesicle suspension, we conclude that the larger objects are likely aggregates and not dust. Furthermore, the polydispersity appears to increase with age of sample, which reinforces the idea that the vesicles are clumping together.

Another indication of the apparent polydispersity is the second cumulant or the standard deviation which is shown as a function of the scattering wavevector in Fig. 5.3. The curve was compared with the results of the polydispersity analysis of the previous chapter to show that the vesicle sample is consistent with a Schulz distribution having a polydispersity parameter of $m = 11$, and a relative standard deviation of 27%. Because of the irregular influence of the larger-sized objects at low q as observed by comparing different vesicle batches, and the anomalous increase at high q, the most representative data points were taken to be from the scattering wavevector midrange.

5.2.2 Effect of Volume Deflation

The hydrodynamic radius as a function of both the scattering wavevector and the deflated volume is shown in Fig. 5.4 for vesicles extruded in 50 mM NaCl solution. The 0% volume decrease represents the vesicles in an iso-osmotic (same initial salt concentration inside and outside the vesicles) solution and does not refer to zero excess area, as explained above. As the vesicle volume was decreased by 20% and by 40%, the hydrodynamic radius was found to decrease, as expected — the vesicles appear to be shrinking as their volume is deflated. With the 75% decrease in volume however, the curve of the radius was found to lie between those of the 20% and the 40%. This suggests a relatively large change in shape for 75% volume-deflated vesicles, a change large enough to significantly affect the manner in which they diffuse. The graph of the second cumulant, as shown in Fig. 5.5, also shows a higher polydispersity for the 75% volume-deflation sample than for the others. As shown in Fig. 5.6, similar results were observed for the radii of volume-deflated vesicles that had been extruded in 100 mM NaCl solution.

Again, the non-zero slope of the radius indicates either polydispersity of the sample or

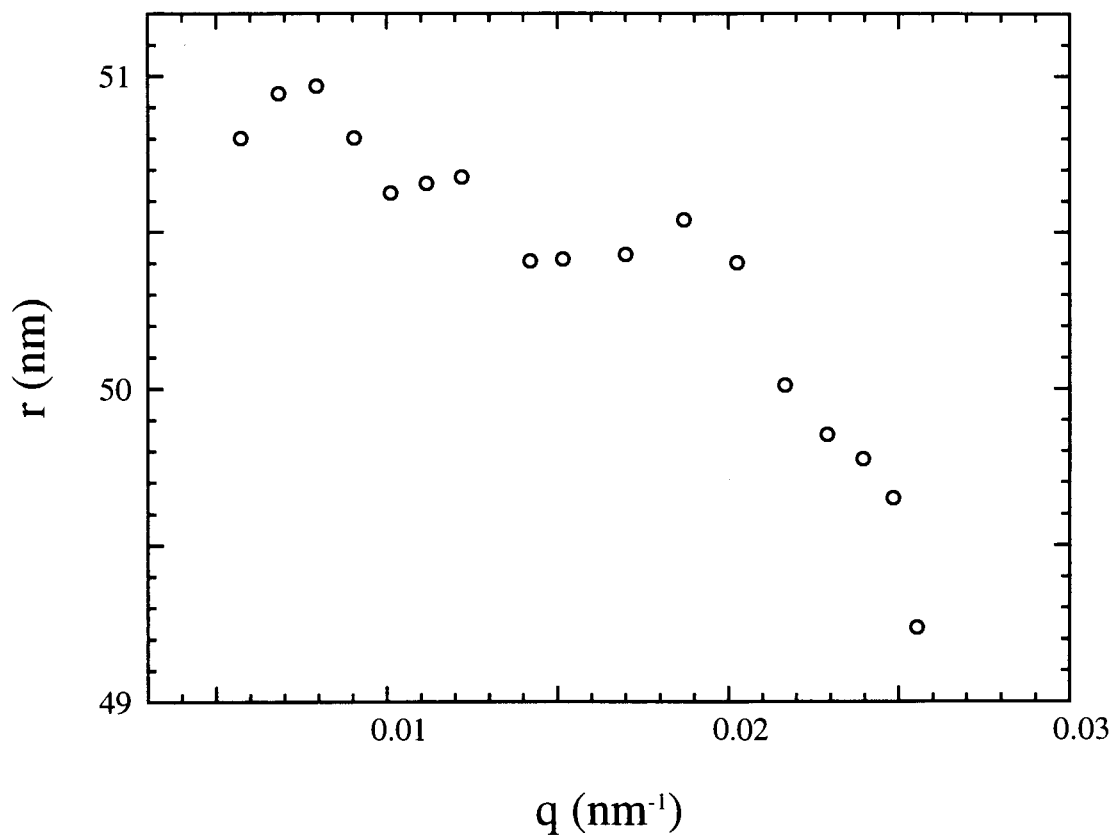

Figure 5.2: The hydrodynamic radius versus the scattering wavevector for DEPC vesicles in de-ionized water at 25°C. The non-zero slope is either indicative of the polydispersity of the sample or something else that can't be distinguished from the polydispersity. Again the error is 1%.

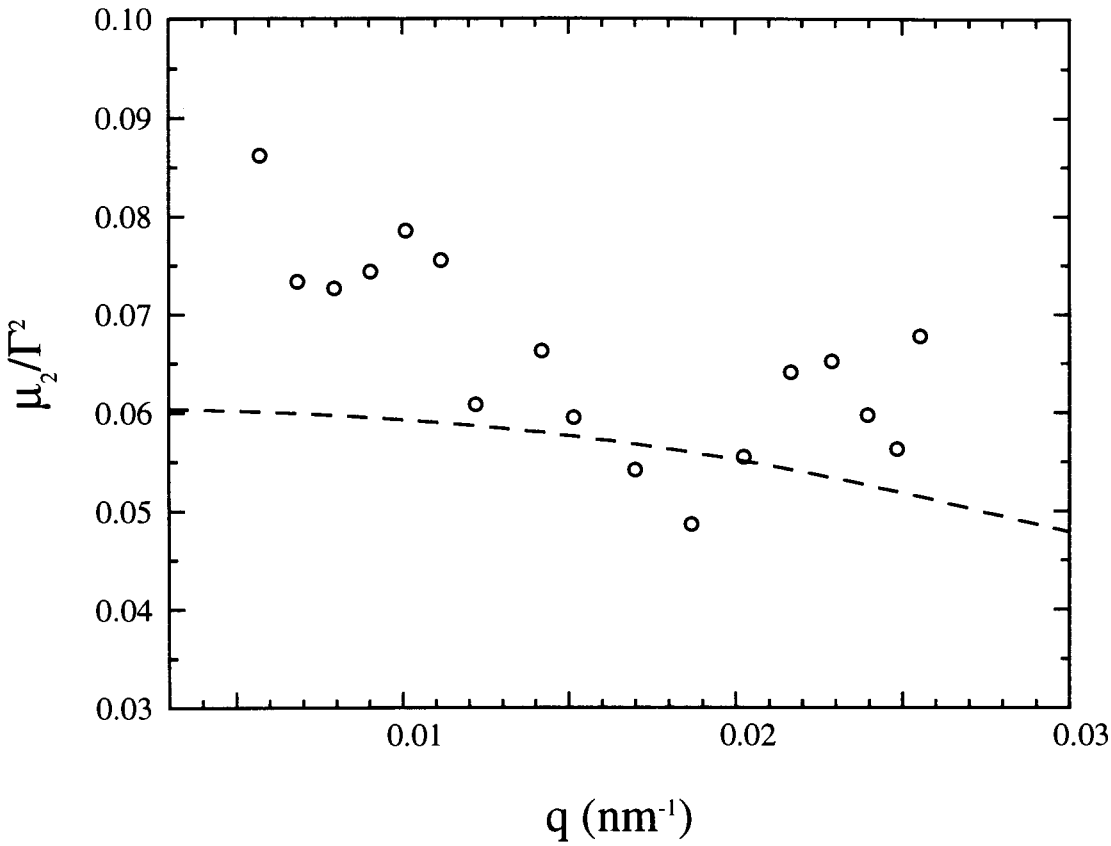

Figure 5.3: The second cumulant, μ_2/Γ^2, as a function of the scattering wavevector from the same analysis of DEPC vesicles in de-ionized water at 25°C as shown in the previous figure. From the analysis described in the previous chapter, the second cumulant or standard deviation of vesicle size is estimated to be 27% and the dotted line is a curve to represent m=11. The data points from the scattering wavevector mid-range were inferred to be the most representative because of the variation in the low q radii between different vesicle batches and the anomalous decrease of the radii at high q.

something else that cannot be distinguished from the polydispersity.

5.2.3 Effect of Salt Concentration

The effect of salt concentration on the hydrodynamic radius was investigated to rule out the possibility that the effect produced by increasing the excess area is actually an effect that is induced by merely increasing the overall salt concentration both inside and outside of the vesicle. As shown in Fig. 5.7, an increased salt concentration generally resulted in an increase of the hydrodynamic radius or a decrease of the diffusion coefficient. This behaviour is opposite to the trend that was found in the volume-deflated vesicles. We can compare the volume-deflated samples with the iso-osmotic samples: for the 75% volume-deflated vesicles in which the final exterior salt concentration for the 50 mM initial salt concentration was 200 mM, the result of the deflation was a 9% decrease in the hydrodynamic radius. For the 50 mM and 200 mM iso-osmotic samples, however, the change from the former to latter of the hydrodynamic radius is a 10% increase. This suggests that the salt concentration alone does not determine the excess area during the extrusion process but that an osmotic difference is needed.

The 100 mM salt concentration vesicles, for a number of different extrusions, were not entirely consistent with the other results and this is an indication of the possible difficulties and nonlinearities of working with phospholipids and charged ions.

5.2.4 Cryo-Electron Microscopy

Samples similar to those used in the volume-deflation experiments, were examined by Dr. Barbara Mui at UBC using an electron microscope at 16000x magnification. This cryo-EM technique involves quickly freezing a thin film of the sample prior to examination under an electron microscope. One experimental problem is the evaporation of the sample prior to freezing which leads to a change in concentration. As shown in Fig. 5.8, the 0% volume-deflated vesicle suspension was found to be very similar to others of the particular salt concentration that have been observed previously (Mui, private communication) . These vesicles, from the electron-micrographs, appear to be a mixture of prolate and oblate shapes. In contrast, the 40% volume decrease seemed to have the effect of "rounding" up the vesicles, as shown in Fig. 5.9. Since there were also what appeared to be edge-on views of disc shapes, it is entirely possible that the suspension was now for the most part, oblate shaped.

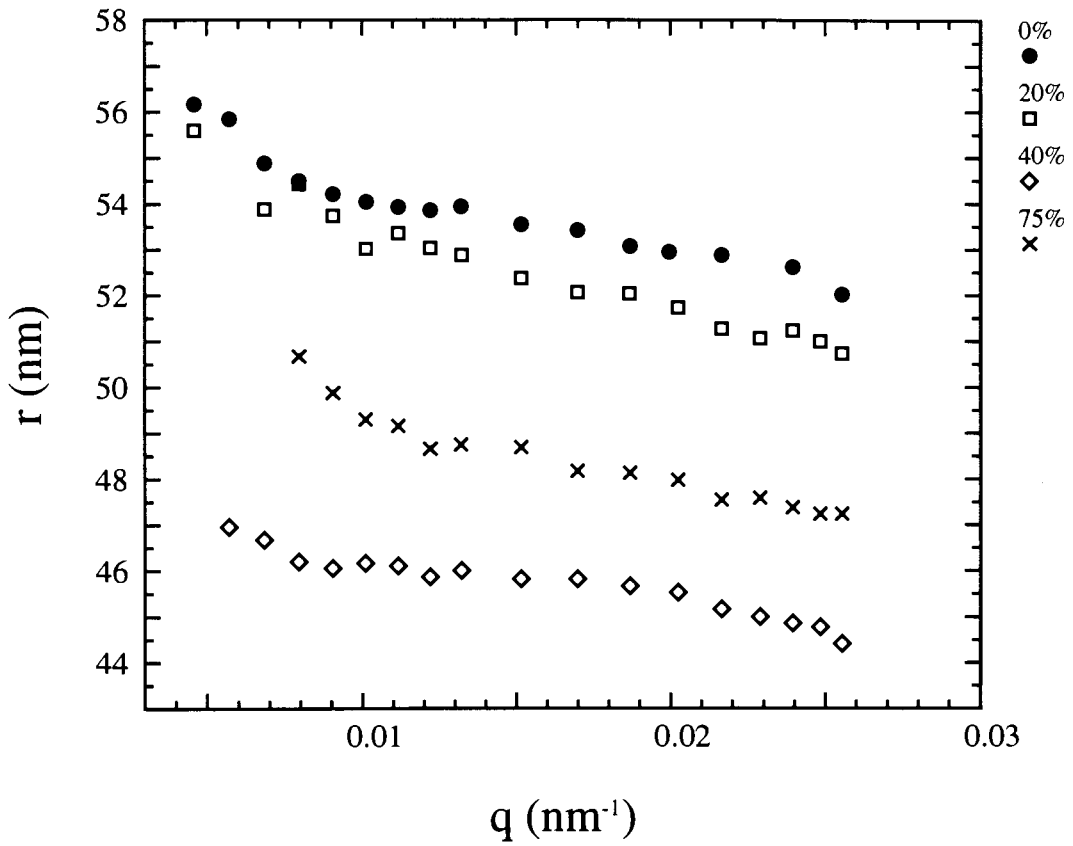

Figure 5.4: The dependence of the hydrodynamic radius as a function of both the scattering wavevector and the decreased volume at 25°C for vesicles initially prepared in 50 mM NaCl solution. Initially, the radii appear to decrease as the vesicle volume is progressively decreased, but the curve for the volume deflation of 75% was found to lie between those of the 20% and 40% curves. Again the negative slope of each radius curve is indicative of the polydispersity of the vesicles. A possible explanation for the upward turn of each curve at low q is the presence of aggregates.

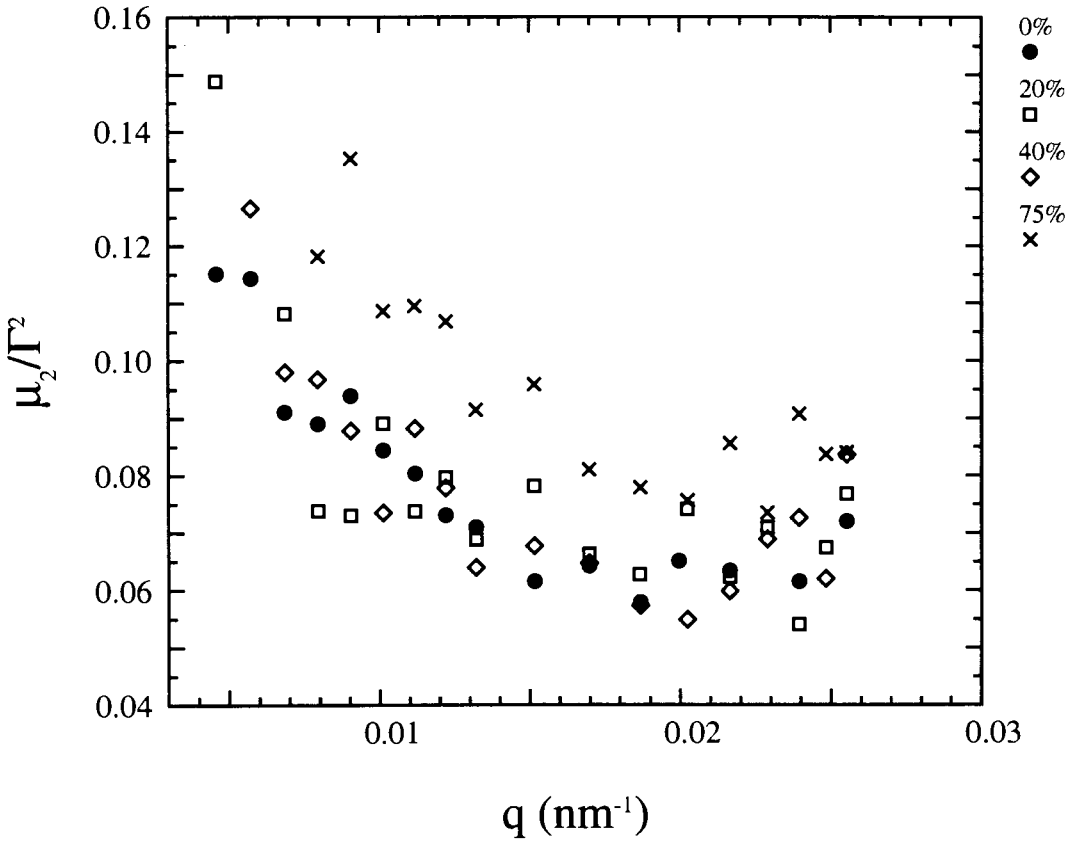

Figure 5.5: The second cumulant μ_2/Γ^2 as a function of scattering wavevector and the percent volume deflation for the same samples as shown in the previous figure (measured at 25°C for vesicles initially prepared in 50 mM NaCl solution). Note that the 75% volume-deflation shows a higher polydispersity than the others.

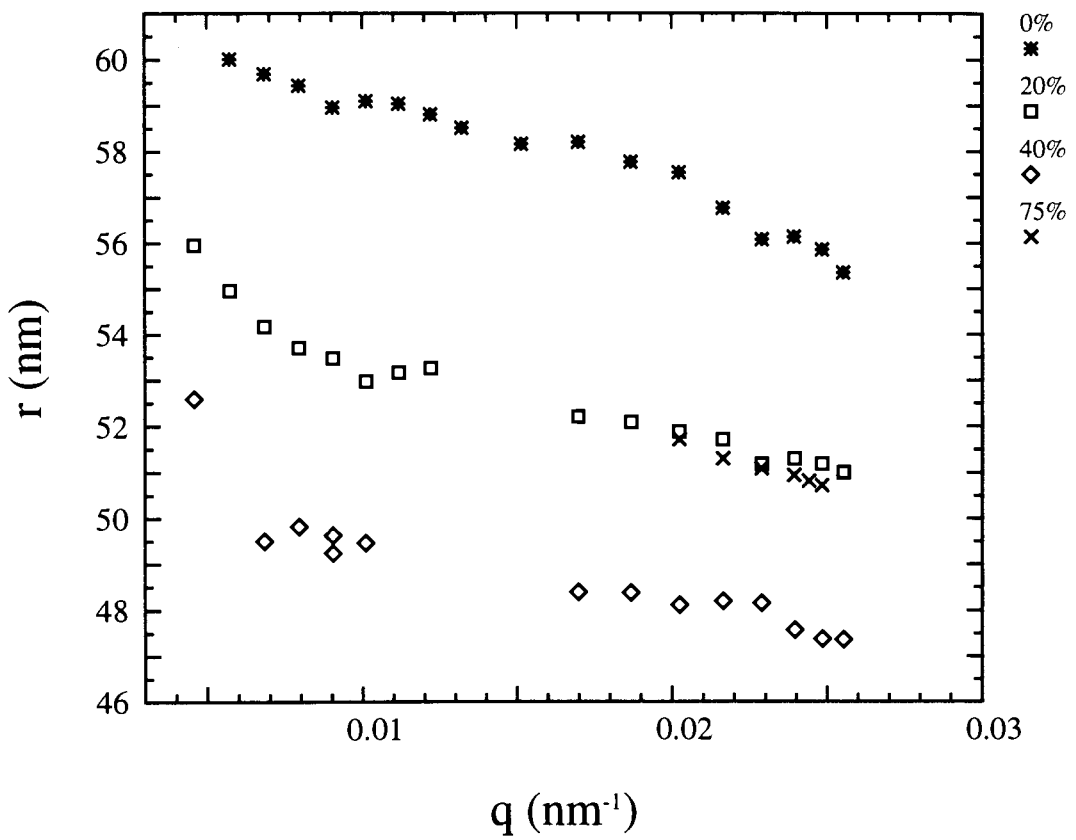

Figure 5.6: The hydrodynamic radius as a function of both the scattering wavevector and the decreased volume at 25°C for vesicles initially prepared in 100 mM NaCl solution. Note that the general trends are similar to those of the volume-deflated vesicles prepared in 50 mM NaCl solution.

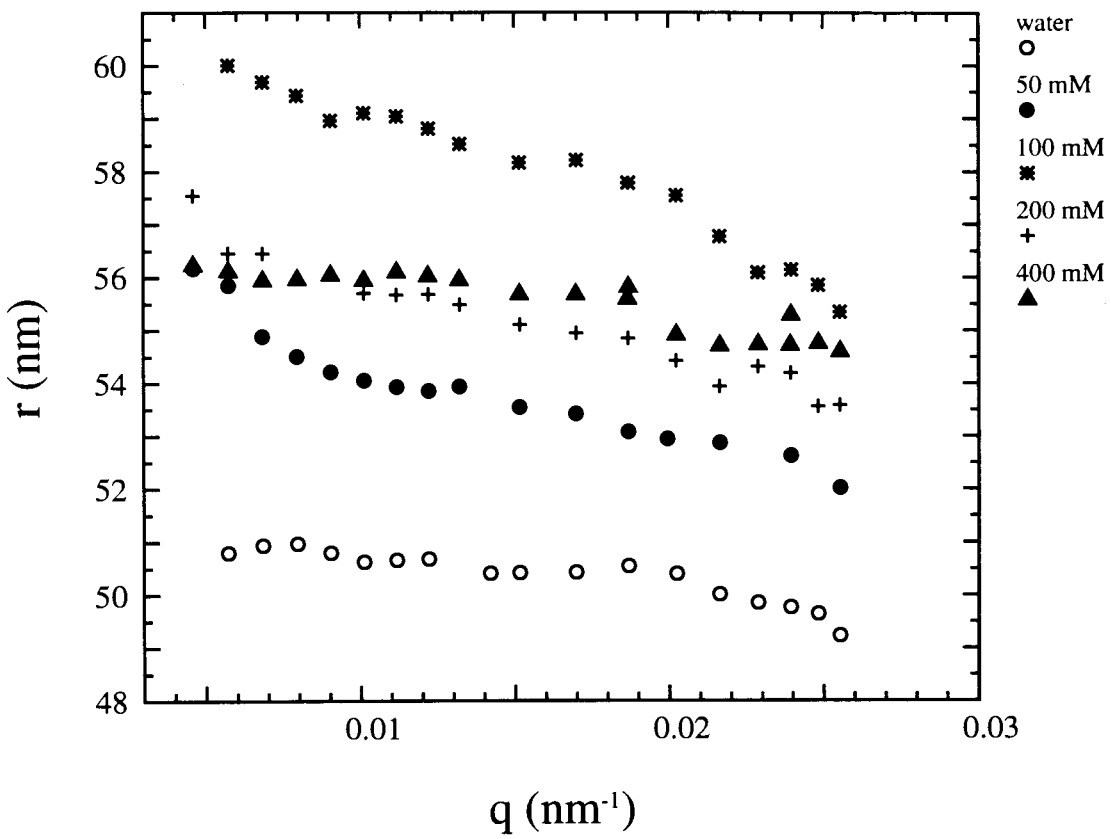

Figure 5.7: The hydrodynamic radius *vs* the scattering wavevector as a function of salt concentration at 25°C. The greater the salt concentration, generally the larger the radius; opposite of the trend observed the volume deflated vesicles. This would suggest that the variation in the hydrodynamic radius as a function of the salt concentration is not an effect of the excess area. The location of the 100 mM salt curve is an indication of possible charge effects introduced by the salt ions that lead to irregularities.

What is unclear though is the progression to the 75% volume-deflated vesicles, as shown in Fig. 5.10. Some difficulty was incurred in properly freezing the sample and this puts into question the micrographs taken for this percentage volume decrease. The vesicle shapes appear to approach bi-concave or invaginated or even toroidal geometries.

5.3 Effect of Viscosity

The time scale of the shape fluctuations is inversely proportional to the viscosity of the suspending fluid, as discussed in Section 2.3. Using water as the suspending fluid, the time scale of fluctuation predicted for the lowest mode of a relevant vesicle size is in the lower limit of detection of our experimental equipment. By increasing the viscosity by a factor of 10, the time scale is placed comfortably in the mid-range of detection. Thus, by increasing both viscosity and the excess area via volume deflation, the probability of detecting the fluctuations should be higher.

DEPC lipid vesicles were hydrated and extruded in a 60% by weight glycerol 50 mM NaCl solution. The viscosity of the suspension was roughly 10 cp at 25°C, 10 times more viscous than ordinary water. The volume of the vesicles was then decreased following the method described previously in Section 5.2. Not one but two different time scales were apparent in the observed correlation function. The dominant decay was again due to the translational diffusion of the vesicles while the second decay was much smaller in amplitude and faster in time. Because the effect was not only visible at low vesicle concentration and was of the same magnitude for all volume deflations (0%, 20%, 40%) but also visible for a glycerol solution, without vesicles, we concluded that this additional timescale was caused by density fluctuations of the glycerol itself.

5.4 Summary of Results

While light-scattering experiments performed on vesicle suspensions showed no evidence of shape fluctuations, they also did not show evidence against shape fluctuations. The methods used to enhance the fluctuations included changing the temperature, increasing the viscosity and increasing the excess area of the vesicles.

By altering the temperature of the DMPC-vesicle suspension, the hydrodynamic radius was measured as a function of temperature and was found to vary with temperature. A

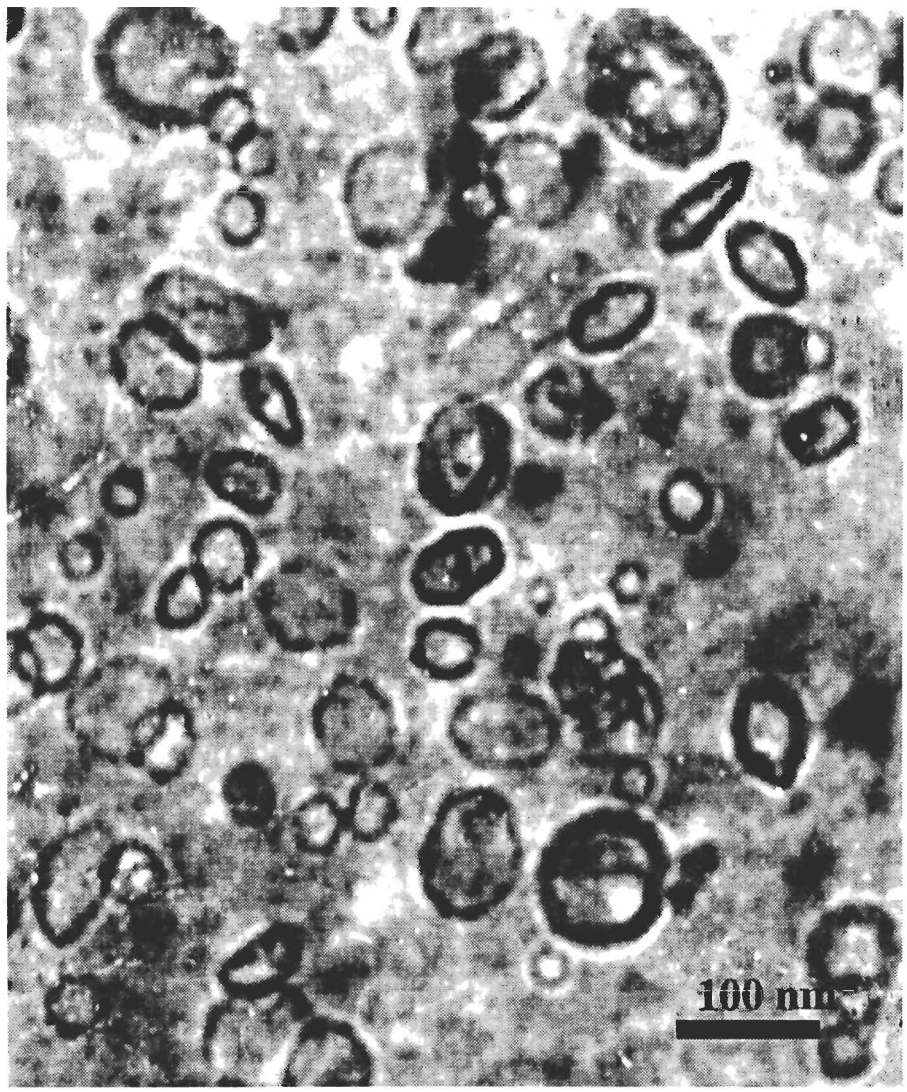

Figure 5.8: The 0% volume-deflated solution: shapes observed include possible prolates and oblates.

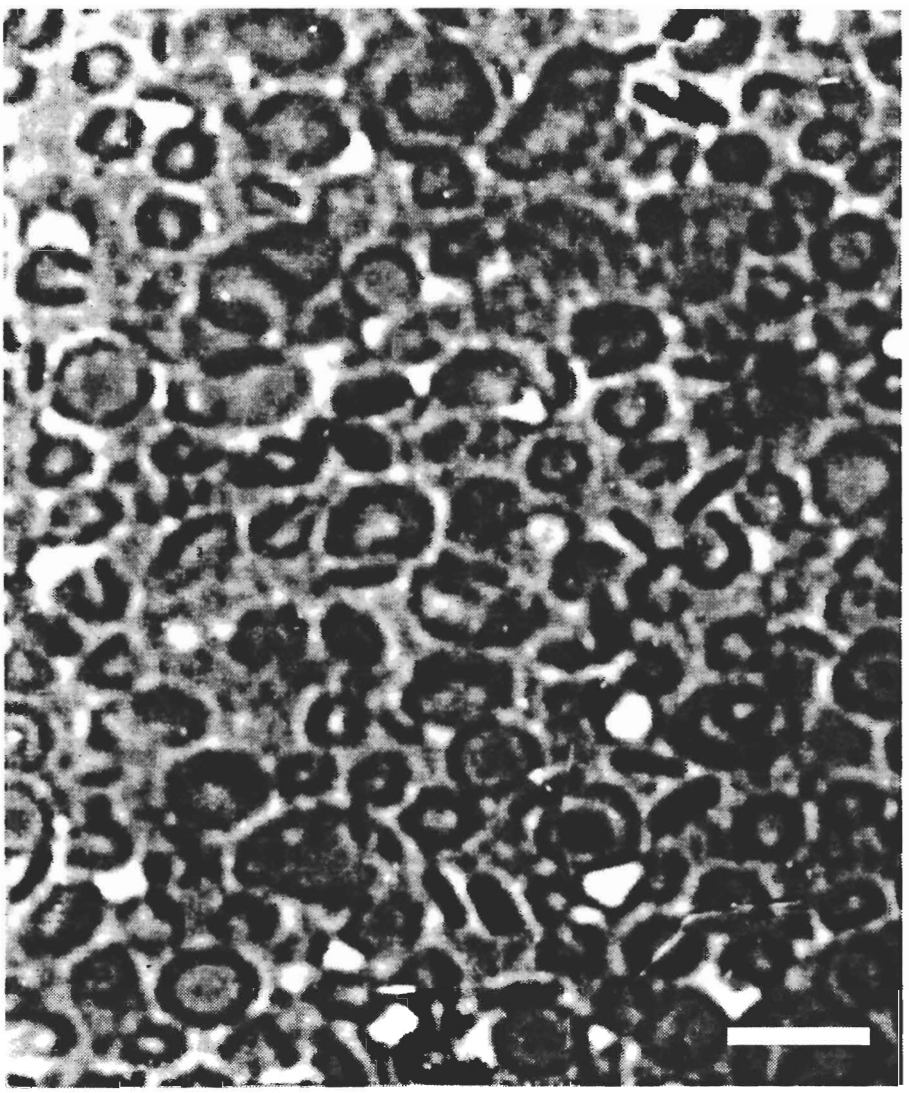

Figure 5.9: The 40% volume-deflated solution: the vesicles, on the whole, are rounder than they appear without volume deflation. The bar represents roughly 100 nm.

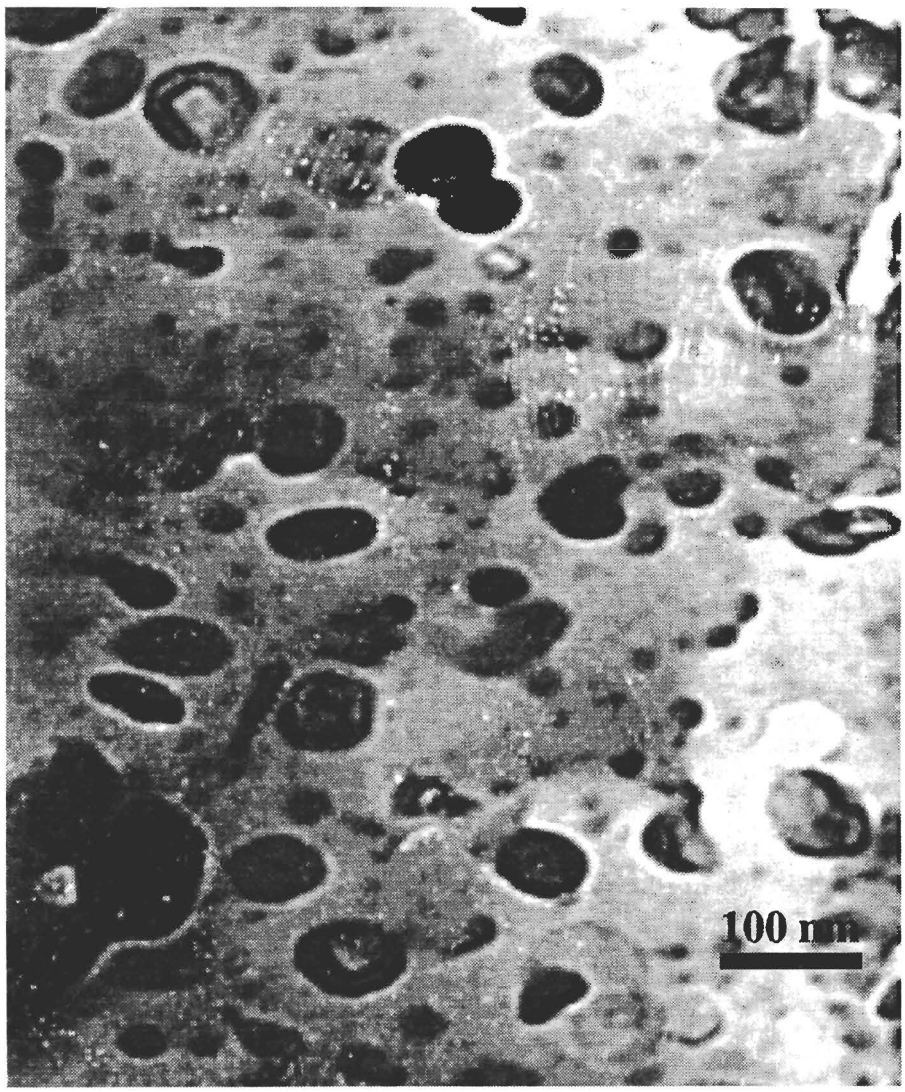

Figure 5.10: The 75% volume-deflated solution: some difficulty was met in freezing the sample. Shapes appear to be quite different than in the previous samples of 0% and 40% volume-deflation.

sharp change in the hydrodynamic radius at 23°C was attributed to the gel transition of the DMPC phospholipid.

The excess area of DEPC vesicles was increased by introducing an osmotic difference between the inside and the outside of the vesicles, and thereby deflating the volume of the vesicle. Initial salt concentrations of 50 mM and 100 mM NaCl were used. Although the vesicle volume was deflated by 20%, 40% and 75%, no evidence was observed to suggest shape fluctuations of the vesicles. However, the hydrodynamic radius was found to decrease with decreasing volumes for the 20% and 40% samples. Curiously, the 75% volume-deflation was anomolous to the trend shown from the other samples. To support the light-scattering data, cryo-EM micrographs showed an assortment of ellipses for the 0% deflation, a much rounder shape for the 40% deflation, and quite deflated shapes for the 75% deflated sample.

The light-scattering data in conjunction with the micrographs would suggest that the volume deflation causes a shape change of the vesicles, and this results in a change of the hydrodynamic radius. From calculations of the change in the diffusion coefficient as a result of a deflated volume, assuming a prolate ellipsoid form, a 20% volume deflation should result in a 1% decrease in the hydrodynamic radius, while a 40% volume deflation should result in a 2% decrease, and a 75% volume deflation should result in a 5% decrease in the hydrodynamic radius (Frisken, private communication). In comparison, the experimental results showed decreases of 2%, 20%, and 9%, respectively, for the hydrodynamic radius.

This difference between the expected values and the experimental values may, in part, be due to assumptions made in the calculation. Not only is a zero initial excess area assumed but the diffusion coefficient was calculated for a hard ellipsoidal (prolate) form. Because it is quite resonable to believe that the vesicle has a large excess area at a 75% volume deflation and this is supported by the micrograph, the diffusion coefficient calculated from a rigid particle may be inappropriate to describe the diffusion of the vesicle. This is a possible indication that the vesicles are undergoing shape fluctuations. However, because of the uncertainty in the initial excess area and form, and the uncertainty in the final form, i.e. prolate or oblate, and the lack of an observable second decay time, this is only one possible hypothesis.

Additional work has been done to reproduce the results of the excess area volume-deflation experiments presented here but there has been little success. Because the vesicle solutions, once extruded, were found to aggregate within a time span of a couple of days, suspensions were often re-extruded. Dr. Barbara Frisken has since observed that the vesicles

are considerably smaller upon re-extrusion and this may be partially the cause of the size differences measured. However, the cryo-EM micrographs, which were taken from samples that had been identically extruded, do suggest a difference between the volume deflations that should be measurable.

The vesicles were also measured for a variety of salt concentrations, to investigate the possible relation between salt concentration and the hydrodynamic radius of the vesicles. It was found that the hydrodynamic radius generally increased with increased salt concentration, which is opposite to the effect observed in the volume-deflated vesicles. This suggests that the salt concentration alone does not determine the excess area but that an osmotic difference is needed. The hydrodynamic radius curve for 100 mM NaCl DEPC vesicles was found to be anomalous to the trend observed for the other salt concentrations. Such an anomaly may be an indication of the possible difficulties of working with ions and phospholipids.

The time scale of the fluctuations was increased away from the threshold of detection by suspending the DEPC vesicles in a more viscous 60% by weight glycerol solution. The excess area was also decreased via volume deflation. Although the fluctuations of the suspension were effectively slowed down by an order of magnitude, no evidence of the shape fluctuations was observed.

The vesicle suspensions were found to be much more polydisperse in size and in shape than had been assumed. The polydispersity is manifested in the width of the distribution as given by the second cumulant and the variation of the diffusion coefficient/hydrodynamic radius with the scattering wavevector. By comparing the second cumulant from experiment with the results obtained from polydispersity analysis using the Schultz distribution, the standard deviation was estimated to be 27%. In addition, electron-micrographs of the vesicles in 50 mM NaCl solution showed not only a distribution of sizes but also a variety of ellipsoidal shapes for the vesicles.

In general, the hydrodynamic radius was found to vary linearly as a function of the scattering wavevector. Sharp upturns of the hydrodynamic radius at small wavevector were attributed to larger structures in the sample, possibly larger vesicles or aggregates. In many of the samples, a downturn of the hydrodynamic radius curve at larger values of the scattering wavevector was also observed. Because this also occurred for the vesicles suspended in de-ionized water, which should be spherical and have no excess area and hence no fluctuations, this anomaly is probably not due to fluctuations. It may be due to smaller

vesicles.

A small number of static-light-scattering measurements were made but because of the small size of the vesicles and the particular range of the scattering wavevector that was available, the emphasis was placed on dynamic-light-scattering measurements instead.

Chapter 6

Conclusion/Discussion

One aspect of artificial vesicles is their usefulness as an experimental means of substantiating the theoretical work done on model membrane systems, and of particular interest are the shape fluctuations of vesicles, which arise from the relatively low bending energy of the bilayer. As the vesicles fluctuate in shape, characteristic time scales can be associated with the different modes of the fluctuations. It was our intent to measure the time scales of the fluctuations with light-scattering methods.

The vesicles were prepared in a variety of ways to increase the likelihood of detection and measurement of the shape fluctuations. By increasing the viscosity of the suspending medium with the addition of glycerol, the fluctuations were slowed down to a more comfortably measureable time scale. And by increasing the temperature, the excess area should increase and thereby increase the amplitude of the fluctuations. Furthermore, by increasing the excess area by altering the relative salt concentrations inside and outside of the vesicles, the amplitude of the fluctuations is increased and so the shape fluctuations should be more easily detected. However, no evidence of fluctuations was observed. We believe that this is due to a number of reasons: the small amplitude of scattering from the vesicles, the polydispersity in size and shape of the vesicle suspension, the small amplitude of the shape fluctuations, and the small size of the vesicles. Very briefly, the signal due to scattering from the vesicles themselves is weak but not difficult to detect. However, it is likely that the shape fluctuations scatter far less light, and are thus much more difficult to detect.

Polydispersity in the size of the vesicles was found to have two important effects: first, both the diffusion coefficient and the standard deviation varied with the scattering wavevector and second, small-amplitude shape fluctuations were obscured. While many researchers

often look for the scattering wavevector dependence of the diffusion coefficient as an indication of surface fluctuations, this is inappropriate for a polydisperse system such the vesicles. Because of the second effect, we endeavoured to minimize the polydispersity. Although the extrusion technique for making vesicle suspensions was chosen for its comparative uniformity of vesicle size distribution and reproducibility, we have determined that the extruded vesicles are not as uniform in size as previously expected. From comparisons of the experimental data with the results of a polydispersity analysis using the Schultz distribution, the vesicle suspension was found to have a 27% standard deviation. In addition, this value was obtained for 100 nM diameter vesicles, with other vesicle sizes having even wider size distributions and more polydispersity. The size distributions of larger vesicles were generally found to be bimodal with one mode centered about the extrusion filter pore size and another around 100 nM. Because the smaller vesicles are always present, filtering does not have the desired effect of reducing the polydispersity of the size distribution for the larger vesicles. Other methods of mechanical separation such as centrifuging and dialysis are also impractical due to the low density of the vesicles and their tendency to aggregate.

While the cryo-EM micrographs of the vesicles show a distribution of sizes, the micrographs also show a distribution of shapes that is not observable in the light scattering data. This shape distribution highlights another aspect of the polydispersity, and that is the variation of excess area from vesicle to vesicle. Since vesicles extruded in salt do not "round up" but remain ellipsoidal, there is not only a polydisperse size distribution but also distribution of excess area or shape. Because a second timescale corresponding to the rotation of asymmetrical shapes such as ellipsoids, either prolate or oblate, is not observed, it would seem that shape variations are obscured by the degree of polydispersity. Another possible contribution to the variation in shape as shown in the micrographs is the shape fluctuations themselves, but if this is the case, we have not been able to detect a related time scale. Hence, either there is not a distinct time scale or the amplitude of the shape fluctuation is very small in relation to that of the translational diffusion.

To estimate how to improve the probability of measuring the shape fluctuations, we first assume a double exponential form for the correlation function, as expressed in Eq. 4.13. Again, one exponential would represent the translational diffusion, while the second exponential would represent the shape fluctution. Empirically, it has been found that two decays are measurable if their amplitudes are such that:

$$A_2 \leq 0.1 A_1 \quad , \tag{6.1}$$

for a double exponential form (Frisken, private communication). By approximating the shape fluctuation amplitude as the difference in the intensity scattered from spherical shells and elliptical shells, as shown in Fig. 4.7, an estimate of the measurable shape fluctuation can be obtained. So, a difference of 10% or more between the intensity scattered by a spherical shell and an elliptical shell should be measurable.

It is important to observe that the shape fluctuation amplitude is then dependent upon the polydispersity of the sample, the scattering wavevector q and the number average radius r. In general, the less polydisperse is the sample, the larger the shape fluctuation amplitude. However, this is also strongly dependent upon the accesible range of qr, with the range of the scattering wavevector being essentially a constant of the experimental apparatus. For the large unilamellar vesicles, (r ~50 nm, $qr \leq 1.3$), that were used in these experiments, it is interesting to note that there is no polydispersity (large or small) at which the shape fluctuation amplitude is larger than 10%. By considering the polydispersity alone, the m=11 value obtained for these vesicles is close to the minimum m value that would allow an observable shape fluctuation amplitude. Recall that the smaller the m value, the larger the polydispersity. By increasing the vesicle size by a factor of two, at the same polydispersity, shape fluctuations should be measureable. In addition, assuming that the relaxation time scales as r^3, from Eq. 2.18, the relaxation time would increase by a factor of eight, and this would be easier to measure. Therefore, to measure the shape fluctuations: the size of the vesicles must first be increased by at least a factor of two, and the vesicles must have either a similar or smaller polydispersity.

One approach to increasing the sensitivity of measurement to the fluctuations is to decrease the relative amplitude of the signal due to translational diffusion. This can be done by making dynamic measurements at the scattering wavevectors q which give the minima of the structure factor for the particular sized vesicles. It is unfortunate that vesicles of the 100 nm size are too small to give a sufficient q range with the existing experimental set-up. Larger vesicles of sizes $r > 150$ nm would permit measurements to be made at the first minimum of the structure factor, at $qr = \pi$; but the polydispersity of these vesicles would greatly reduce both the sharpness of the minimum and effectiveness of this method.

In conclusion, we were unable to measure the size and shape fluctuations of vesicles because of the obscuring effects of the polydispersity of the vesicles, the small amplitude of fluctuations, and the small size of the vesicles.

Bibliography

[1] S.R. Aragón and R. Pecora, "Theory of dynamic light scattering from polydisperse systems", J. Chem. Phys. **64**, 2395 (1976).

[2] B.J. Berne and R. Pecora, *Dynamic Light Scattering*, (Robert E. Krieger Publishing Company, Florida, 1976).

[3] F. Brochard and J.F. Lennon, "Frequency spectrum of the flicker phenomenon in erythrocytes", J. Phys (France **36**, 1035 (1975).

[4] N.A. Clark, J.H. Lunacek, and G.B. Benedek, "A study of Brownian motion using light scattering", Am. J. Phys. **38**, 575 (1970).

[5] S.G. Clerc, and T.E. Thompson, "A possible mechanism for vesicle formation by extrusion", Biophys. J. **67**, 475 (1994).

[6] B.A Cornell, G.C. Fletcher, J. Middlehurst, and F. Separovic, "Temperature dependence of the size of phospholipid vesicles" Biochim. Biophys. Acta **642**, 375 (1981).

[7] P. Cullis, private communication, (1994).

[8] V. Degiorgio and J.B. Lastovka, "Intensity-Correlation Spectroscopy", Phys. Rev. A **4**, 2033 (1971).

[9] H.-G. Döbereiner, W.Rawicz, M.Wortis, and E.Evans, unpublished.

[10] J.P. Duwe, J. Käes, and E. Sackmann, "Bending elastic moduli of lipid bilayers : modulation by solutes", J. Phys. (France) **51**, 945 (1990).

[11] E. Evans and D. Needham, "Physical properties of surfactant bilayer membranes: thermal transitions, elasticity, rigidity, cohesion, and colloidal interactions", J. Chem. Phys. **91**, 4219 (1987).

[12] B. Farago, D. Richter, and J.S. Huang, "Shape fluctuation of microemulsion droplets", Physica B **156** & **157**, 452 (1989).

[13] B.J. Frisken, private communication, (1994).

[14] S. Fujime, M.T.-Ohsita, and S. Miyamoto, "Dynamic light scattering from polydisperse suspensions of thin ellipsoidal shells of revolution with submicron diameters", Biophys. J. **53**, 497 (1988).

[15] H. Gang, A.H. Krall, and D.A. Weitz, "Shape fluctuations of interacting fluid droplets", preprint.

[16] E.F. Grabowski and J.A. Cowen, "Thermal excitations of a bilipid membrane", Biophys. J. **18**, 23 (1977).

[17] F.R. Hallett, J.Marsh, and B.Nickel, "Mechanical properites of vesicles. II. A model for osmotic swelling and lysis", Biophys. J. **64**, 435 (1993).

[18] W. Helfrich, "Size distributions of vesicles: the role of the effective rigidity of membranes", J. Phys. (France) **47**, 321 (1986).

[19] W. Helfrich, "Elastic properties of lipid bilayers: theory and possible experiments", Z. Naturforsch. **28 c**, 693 (1973).

[20] M.J. Hope, M.B. Bally, G. Webb, and P.R. Cullis, "Production of large unilamellar vesicles by a rapid extrusion procedure. Characterization of size distribution, trapped volume and ability to maintain a membrane potential", Biochim. Biophys. Acta **812**, 55 (1985).

[21] J.S. Huang, S.T. Milner, B. Farago, and D. Richter, "Study of dynamics of microemulsion droplets by neutron spin-echo spectroscopy", Phys. Rev. Lett. **59**, 2600 (1987).

[22] E.W. Kaler, K.L. Herrington, and A.K. Murthy, "Phase behaviour and structures of mixtures of anionic and cationic surfactants", J. Phys. Chem. **96**, 6698 (1992).

[23] D.E. Koppel, "Analysis of macromolecular polydispersity in intensity correlation spectroscopy: the method of cumulants" J. Chem. Phys. **57**, 4814 (1972).

[24] W. Li and T.H. Haines, "Uniform preparations of large unilamellar vesicles containing anionic lipids", Biochem. **25**, 7477 (1986).

[25] S.T. Milner and S.A. Safran, "Dynamical fluctuations of droplet microemulsions and vesicles", Phys. Rev. A **36**, 4371 (1987).

[26] B.L.-S. Mui, P.R. Cullis, E.A. Evans, and T.D. Madden, "Osmotic properties of large unilamellar vesicles prepared by extrusion", Biophys. J. **64**, 443 (1993).

[27] B.L.-S. Mui, private communication, (1994).

[28] F. Olson, C.A. Hunt, F.C. Szoka, W.J. Vail, and D. Papahadjopoulos, "Preparation of liposomes of defined size distribution by extrusion through polycarbonate membranes." Biochim. Biophys. Acta. **557**, 9 (1979).

[29] M.A. Peterson, "Shape dynamics of nearly spherical membrane bounded fluid cells", Mol. Cryst. Liq. Cryst. **127**,257 (1985).

[30] W. Press, *Numerical Recipes in C: The Art of Scientific Computing*, (Cambridge University Press, New York, 1992).

[31] S.W. Provencher, "A constrained regularization method for inverting data represented by linear algebraic or integral equations", Comp. Phys. Comm. **27**, 213 (1982).

[32] S.W. Provencher, "CONTIN: a general purpose constrained regularization program for inverting noisy linear algebraic and integral equations", Comp. Phys. Comm. **27**, 229 (1982).

[33] H. Ruf, "Effects of normalization error on size distributions obtained from dynamic light scattering data", Biophys. J. **56**, 67 (1989).

[34] M.B. Schneider, J.T. Jenkins, and W.W. Webb, "Thermal fluctuations of large quasi-spherical bimolecular phospholipid vesicles", J. Phys. (France) **45**, 1457 (1984).

[35] M.S. Webb, C.P.S. Tilcock, and B.R. Green, "Salt-mediated interactions between vesicles of the thylakoid lipid digalactosyldiacylglycerol", Biochim. Biophys. Acta **938** 323, (1988).